CHAPTER 1

Type-II Superlattice Infrared Detectors

David Z.-Y. Ting, Alexander Soibel, Linda Höglund, Jean Nguyen, Cory J. Hill, Arezou Khoshakhlagh, and **Sarath D. Gunapala**

Contents

Semiconductors and Semimetals, Volume 84
ISSN 0080-8784, DOI: 10.1016/B978-0-12-381337-4.00001-2

1. INTRODUCTION

The type-II InAs/GaSb superlattices (Sai-Halasz *et al.*, 1977) have several fundamental properties that make them suitable for infrared detection: their band gaps can be made arbitrarily small by design (Sai-Halasz *et al.*, 1978a), they are more immune to band-to-band tunneling compared with bulk material (Smith and Mailhiot, 1987; Smith *et al.*, 1983), the judicious use of strain in type-II InAs/GaInSb strained layer superlattice (SLS) can enhance its absorption strength over that of the type-II InAs/GaSb superlattice to a level comparable with HgVdTe (MCT) (Smith and Mailhiot, 1987), and furthermore, type-II InAs/Ga(In)Sb superlattices have been shown theoretically (Grein *et al.*, 1992) and experimentally (Youngsdale *et al.*, 1994) to have reduced Auger recombination. These properties generated strong interests and led to the demonstration of the first high-performance photodiodes (Fuchs *et al.*, 1997a; Johnson *et al.*, 1996) and focal plane array (FPA) (Walther *et al.*, 2005b). In the mid-wavelength infrared (MWIR), sophisticated production-ready simultaneous dual-band FPAs already exist (Rehm *et al.*, 2010; Walther *et al.*, 2007). In the long-wavelength infrared (LWIR), heterostructure superlattice detectors (Aifer *et al.*, 2010a; Gautam *et al.*, 2010; Nguyen *et al.*, 2007b; Ting *et al.*, 2009a) that effectively use unipolar barriers (Ting *et al.*, 2009a) have shown strong reduction of generation-recombination (G-R) dark current due to Shockley-Read-Hall (SRH) processes. Higher absorber doping levels afforded by immunity to tunneling has led to reduced diffusion dark current (Ting *et al.*, 2010), despite relatively short lifetimes found in existing superlattice material (Connelly *et al.*, 2010; Donetsky *et al.*, 2010; Pellegrino and DeWames, 2009). The dark current characteristics of type-II superlattice-based single element LWIR detectors are now approaching that of the state-of-the-art MCT detector. Noise measurements highlight the need for surface leakage suppression (Soibel *et al.*, 2010), which can be tackled by improved etching (Nguyen *et al.*, 2010b), passivation (Fuchs *et al.*, 1998a; Mohseni *et al.*, 1999), and device design (Aifer *et al.*, 2007; Wicks *et al.*, 2010). Large-format LWIR FPAs have been demonstrated in research laboratories (Gunapala *et al.*, 2010; Manurkar *et al.*, 2010). The continuous improvement in substrate, material quality, device design, and processing technique, coupled with better understanding of the fundamental properties, could lead to high-performance large-format LWIR focal plane arrays in the near future.

The reminder of this chapter is organized as follows: Section 2 reviews the development of the type-II superlattice infrared detectors from a historical perspective. Section 3 discusses basic properties of the type-II superlattice, largely from simple theoretical considerations. Section 4 describes the principles behind advanced superlattice infrared detectors based on heterostructure designs. Section 5 explores some aspects of device fabrication

and characterization of contemporary interest. A short summary and outlook is given in Section 5. As this chapter covers only a limited set of topics, the interested readers are also referred to review articles by Bürkle and Fuchs (2002); Fuchs *et al.* (1997b), and Razeghi and Mohseni (2002), as well as the book by Rogalski (2011) for additional information.

2. HISTORICAL PERSPECTIVE

In this section, we review the development of type-II antimonide superlattice infrared detector through a historical perspective. We begin with the discovery of the broken-gap band alignment and the invention of the type-II superlattice from 1976 to 1978. We next examine the period between 1979 and mid-1990s when the concept of using type-II superlattices for infrared detection took shape, supported by theoretical and experimental works. The following period, between 1996 and 2005, saw the first high-performance detectors and the demonstration of the first focal plane array. Finally, rapid growth of the field occurred between 2005 and the present time (2010), with the emergence of detectors based on advanced heterostructure designs, and significant progress in focal plane array technology development.

2.1. Type-II superlattice and the broken-gap band alignment

The year 1977 marked the birth of the type-II superlattice with the publication of a seminal paper by Sai-Halasz *et al.* (1977) from the IBM T. J. Watson Research Center. In the paper, the authors proposed and analyzed theoretically a new type of bilayer semiconductor superlattice in which the lower conduction band (CB) edge is located in one material, whereas the higher valence band (VB) edge is in the other. In this kind of superlattice (Fig. 1.1), the wave functions of the lowest conduction subband and the highest valence subband are localized in the two different

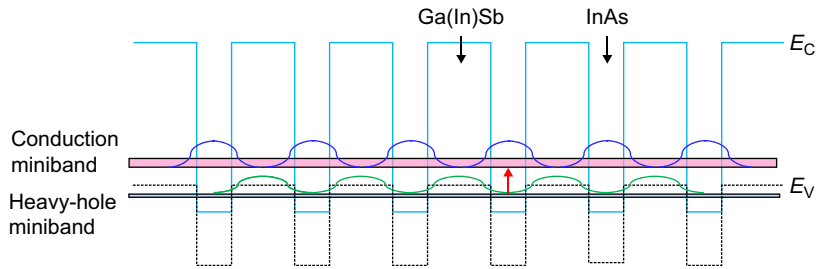

FIGURE 1.1 Schematic illustration of an InAs/Ga(In)Sb type-II broken-gap superlattice showing the spatial separation of the conduction band and the heavy-hole band wave functions. The infrared transition is indicated by an arrow.

host semiconductors (spatially delocalized), and therefore, the positions of the CB edge and the VB edge can be, to first order, tuned independently. It was suggested that this type of superlattice could be realized by using the closely lattice-matched semiconductor pairs of InAs/GaSb or InGaAs/GaSbAs. It was also pointed out in particular that based on the known electron affinity values, the CB edge of InAs was expected to be 0.14 eV lower than the VB edge of GaSb (now called the broken-gap band alignment), and this would lead to an interesting behavior since the superlattice CB and VB states are close in energy and could therefore interact. This new type of superlattice, in which the band gaps of the two host semiconductors are in either a staggered or a broken-gap alignment, was later referred to as "type II" (Sai-Halasz *et al.*, 1978b) to distinguish it from the "type I" superlattice originally proposed by Esaki and Tsu (1970), in which the host band gaps are in a nested alignment.

The key feature that enabled the concept of the type-II superlattice was the broken-gap band alignment between InAs and GaSb. W. Frensley first noticed the very unusual band alignment between InAs and GaSb in the course of his PhD thesis research under the direction of H. Kroemer at the University of Colorado (Frensley and Kroemer, 1977). The IBM Group came to the realization around the same time. Noting the unusually large electron affinity of InAs, Sai-Halasz *et al.* (1977) predicted the broken-gap band lineup between InAs and GaSb based on the electron-affinity rule (Anderson, 1962), which, though later found to be inadequate (Niles and Margaritondo, 1986), happened to hold up well in this case. The InAs-GaSb broken-gap band lineup was also predicted through the means of more sophisticated theoretical methods, as reported by Harrison (1977) using linear combination of atomic orbital (LCAO) theory and by Frensley and Kroemer (1977) using pseudopotential theory. Although Harrison did not attach any special significance to the broken gap alignment (it was one of many values tabulated in a comprehensive study of heterojunction band offsets), Frensley and Kroemer (1977) pointed out that among all the predicted band offsets, perhaps the most interesting is that for the InAs-GaSb system, in which the InAs conduction band edge was predicted to be below that of the GaSb valence band edge. They speculated that this band lineup could lead to very interesting transport properties such as interband tunneling. Indeed, interband tunneling was observed experimentally by Sakaki *et al.* (1977) from IBM in a study of InGaAs-GaSbAs heterojunction diode current–voltage ($I-V$) characteristics.

In the original study of type-II superlattices, Sai-Halasz *et al.* (1977) used Kane's two-band model (Kane, 1957) to treat the interaction between the InAs conduction band and the GaSb light-hole band while ignoring the heavy-hole band. In the following year, Sai-Halasz and Esaki, in

collaboration with Harrison, reexamined the band structure of InAs-GaSb superlattices using LCAO theory (Sai-Halasz *et al.*, 1978a). They found that while superlattices with thin InAs and GaSb layers have well-defined energy band gaps and act as semiconductors, those with thick layers behave as semimetals. This means that the band gap of the InAs/GaSb superlattice can be made arbitrarily small — smaller than that of either InAs or GaSb. The IBM Group then proceeded to demonstrate this trend of decreasing band gap with increasing layer thickness experimentally (Sai-Halasz *et al.*, 1978b) using a set of molecular beam epitaxy (MBE) grown samples that showed measured band gaps ranging from 265 to 360 meV at 10 K. Correlation with theoretical calculations also established the InAs CB edge to be at approximately 150 meV below the GaSb VB edge, a value that is still used today.

In the literature, "type-II broken gap" is sometimes referred to as "type III" to distinguish it from "type-II staggered" (Davies, 1998; Dragoman and Dragoman, 2002; Sze and Ng, 2007). However, the term "type III" is often used in the infrared detector literature to refer to superlattices consisting of alternating layers of an inverted band structure zero-gap semiconductor and a normal wider gap semiconductor, such as the HgTe/CdTe superlattice (Kinch, 2007). Kroemer advocates using only the descriptive names of nested (or straddling), staggered, and broken gap (or misaligned) and doing away with numerical designation of types I, II, and III altogether. We use "type-II broken gap" or simply "type II" in this work.

2.2. Superlattices for infrared detection

The concept of using superlattices for infrared detection started in the HgCdTe (MCT) material system. Although a practical MCT superlattice infrared detector has not been realized, the idea had a major influence on the development of antimonide superlattice infrared detectors. Schulman and McGill (1979a,b) first proposed the use of the CdTe/HgTe superlattice as an infrared material, with possible uniformity advantages over the MCT alloy. In one of their papers, Schulman and McGill (1979a) pointed out that the InAs/GaSb superlattice should have similar band gap properties as the CdTe/HgTe system, but they also expressed the concern that the size of the optical matrix element may be inadequate because electron and hole wave functions of the states involved in the infrared transitions are spatially separated in a type-II superlattice. Later, Smith *et al.* (1983) revisited the theory of CdTe/HgTe superlattices and identified some key advantages of superlattices over bulk materials for infrared detection: (1) the cutoff wavelengths of MCT superlattices have weaker dependence on composition than the MCT alloy and are, therefore, less susceptible to

variations due to compositional fluctuation, (2) superlattices have reduced p-side diffusion current due to the larger electron mass, and (3) superlattice tunneling lengths are shorter than for MCT alloys with the same band gap and therefore have reduced band-to-band tunneling. These properties are found in the InAs/GaSb superlattice as well. Regarding the concern for possible weak oscillator strength in type-II superlattices (Schulman and McGill, 1979a), Chang and Schulman (1985) calculated optical properties of InAs/GaSb superlattices. They found that in a (M,N)-InAs/GaSb superlattice (each period consisting of M monolayers of InAs and N monolayers of GaSb), for sufficiently large M and N (>10 or more), the oscillator strength of optical transitions is approximately proportional to $1/MN$, decreasing rapidly with layer thickness. In a review article, Kroemer (2004) described this in a simple intuitive manner. Since electron and hole wave functions are separately localized in InAs and GaSb layers, respectively, they overlap each other mostly near the heterointerfaces. Hence, to first order, the optical absorption is proportional to the number of interfaces rather than to the superlattice thickness. This means that much of the volume is optically inactive in InAs/GaSb superlattices with long periods (which are needed to achieve small band gaps for long wavelength infrared detection).

So, how can we reduce the superlattice period to enhance oscillator strength without increasing the energy band gap? To address this issue, Smith and Mailhiot (1987) proposed the type II InAs/GaInSb strained layer superlattice (SLS) infrared detector. Smith and Mailhiot considered a free-standing InAs/$Ga_{0.6}In_{0.4}Sb$ SLS in which the InAs and GaInSb layers are under tensile and compressive strain, respectively. As illustrated in Fig.1.2, the effect of strain is to lower the InAs CB edge and raise the GaInSb heavy-hole (HH) band edge, which makes both the InAs CB quantum well and the GaInSb HH band quantum well deeper. Consequently, one could employ narrower quantum wells without increasing the superlattice band gap. The SLS has larger optical matrix elements than the InAs/GaSb superlattice. Although the optical matrix element of the type-II SLS is still smaller than that in bulk MCT, its absorption coefficient is comparable to that of MCT because of the higher joint density of states. The electron effective mass for a 10-μm cutoff SLS is ~0.04 m_0 (0.0088 m_0 for MCT of comparable cutoff wavelength), which is large enough to reduce band-to-band tunneling and still small enough to provide good electron mobility. It was suggested that since electron mobility is much higher than hole mobility, n on p diodes should be used for infrared detection. Smith and Mailhiot also noted that GaSb would be a good substrate on which to grow the InAs/GaInSb superlattice. Miles *et al.* (1990) experimentally demonstrated LWIR absorption in InAs/GaInSb strained layer superlattices.

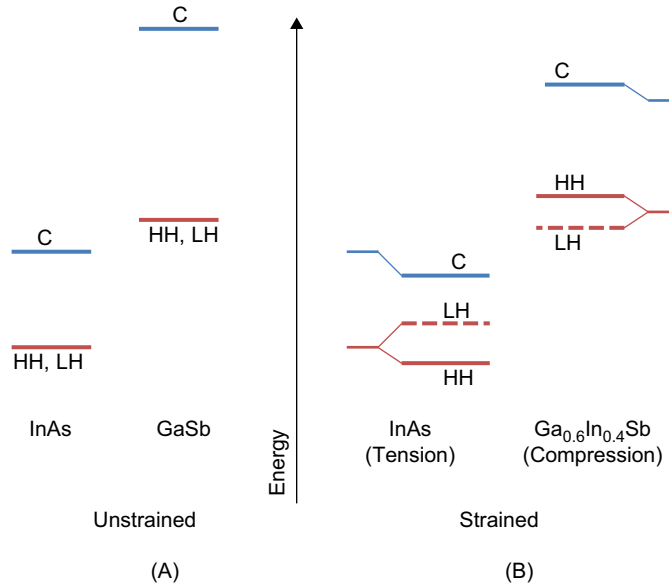

FIGURE 1.2 Band edge energy positions for (A) unstrained InAs and GaSb and (B) strained InAs and $Ga_{0.6}In_{0.4}Sb$ in a free-standing InAs/GaInSb superlattice, after Smith and Mailhiot (1987).

As pointed out by Chow *et al.* (1991), D. L. Smith also postulated that Auger recombination rates in some superlattices should be lower than those in bulk semiconductors due to the splitting of the heavy-hole (HH) and light-hole (LH) bands and the larger electron effective mass. Smith communicated the idea to McGill, who in turn stimulated H. Ehrenreich's group at Harvard to perform detailed calculations to put this concept on a firm theoretical basis. Grein *et al.* (1992) presented a theoretical analysis that showed that *p*-type Auger lifetimes in a 11-μm cutoff InAs/InGaSb SLS at 77 K could be three to five orders of magnitude longer than those of bulk MCT with the same gap (Grein *et al.*, 1992). Experimental measurements of Auger lifetime enhancement in InAs/GaInSb superlattices were reported by Youngsdale *et al.* (1994). As the material quality of antimonide superlattices improves and defect-related dark currents decrease, the long Auger lifetimes could yield real advantages in LWIR antimonide superlattice detectors. Some of the other fundamental studies that are important for the development of the type-II superlattice as an infrared material include the theoretical calculation of InAs/GaSb electronic and optical properties using a realistic band structure model that included band mixing effects (Chang and Schulman, 1985; Schulman and Chang, 1985),

the influence of interface types (Miles *et al.*, 1993), and cross-sectional scanning electron microscopy studies of antimonide superlattices (Feenstra *et al.*, 1994a,b; Lew *et al.*, 1998; Steinshnider *et al.*, 2000b,a).

We note that the term *strained* layer superlattice (SLS) is sometimes used in the literature to refer to both the InAs/GaSb and the InAs/GaInSb superlattices. SLS was originally intended for the InAs/GaInSb superlattices, in which the GaInSb layers are intentionally strained for the purpose of increasing oscillator strength (Smith and Mailhiot, 1987). The slight lattice mismatch (0.6%) between InAs and GaSb was not considered significant in the InAs/GaSb superlattice as the effects on electronic and optical properties are minimal. In this work, we reserve the term SLS for the InAs/GaInSb superlattices. However, we note that the small lattice mismatch between InAs and GaSb can cause sufficient strain build up to affect the material quality in thick InAs/GaSb superlattices. When InAs/GaSb superlattices are grown on GaSb substrates, InSb-like interfaces are often used to provide strain relief. The same interface engineering techniques can also be applied to minimize the average strain in the InAs/GaInSb SLS as has been demonstrated by the work from the Fraunhofer IAF (Fuchs *et al.*, 1997a). It is interesting to note that while the oscillator strength of the InAs/GaSb superlattice is not as strong as that of the InAs/GaInSb SLS, both types of antimonide superlattices are being actively investigated today. In particular, Professor Razeghi's group at the Northwestern University has been reporting results on the InAs/GaSb superlattice since 1998 (Mohseni *et al.*, 1998b,a). Although the oscillator strength of the InAs/GaSb SL is weaker, like its InAs/GaInSb SLS counterpart it also has a higher joint density of states than bulk semiconductors and therefore has an adequately large absorption coefficient. The InAs/GaSb superlattice, which uses unstrained and minimally strained binary semiconductor layers, may also have material quality advantages over the SLS, which uses a strained ternary semiconductor (GaInSb).

2.3. Superlattice infrared detectors and focal plane arrays

During the next development period, roughly from 1996 to 2005, there was important progress in the SL detector technology that made the realization of the first generation of high-performance antimonide-based SL detectors and focal plane arrays (FPAs) possible. During this time, the development of superlattice-based photodetectors has been performed mainly in universities and government laboratories. This period began with the demonstration of high-performance InAs/GaInSb SLS LWIR photodiodes (Fuchs *et al.*, 1997a; Johnson *et al.*, 1996) that generated strong interests in the antimonide superlattices and culminated in the demonstration of the first 256 $\times$ 256 FPA (Walther *et al.*, 2005b). Significant advances

in growth, characterization, design and fabrication were achieved during this time. Even though we will discuss progress in these technological areas individually, the overall progress in each and all of these areas was crucial for improving detector performances. In particular, the importance of material quality and of proper fabrication techniques for achieving high-performance devices was recognized early on (see, e.g., Fuchs *et al.*, 1999). It is important to note that attention to superlattice material has been driven not only by photodetectors but also by infrared lasers.

The improved understanding of the proper growth conditions for superlattices was one of the major achievements during this time period. One aspect that makes the growth of the Sb-based superlattices challenging is the absence of common atoms across the InAs/GaSb heterointerface. Two types of interface layers, InSb-like and GaAs-like, can be formed. A detailed study of the structural properties of InAs/GaSb superlattices with different interface types was performed and showed the advantages of InSb-like interfaces for achieving superior SL structural properties (Herres *et al.*, 1996). Detailed investigations of As/Sb exchange across heterointerfaces, which affects interface roughness and material composition, helped to identify the growth conditions for achieving smooth interfaces (Xie *et al.*, 1999). Interface properties were further investigated using cross-sectional scanning tunneling microscopy to reconstruct antimony segregation that affects compositional grading and interface roughness (Steinshnider *et al.*, 2000b,a). Cross-sectional STM was also used to investigate the atomic scale interface morphology of InAs/(GaIn)Sb superlattices grown by MBE showing a semiquantitative correlation between atomic scale interface structure and transport properties in these structures (Lew *et al.*, 1998). Several studies of SL growth conditions including dependence of interface quality on growth temperatures, effects of group V to group III beam equivalent pressure ratio on surface morphology, and variation of residual doping type and concentration with growth temperature were performed (Bennett *et al.*, 1999; Bürkle *et al.*, 2000; Fuchs *et al.*, 1999). Moreover, growth studies of different antimonide materials, such as AlSb and InAlSb, which are of interest for SL heterostructure development, were conducted (Bracker *et al.*, 2001; Plis *et al.*, 2003).

High-quality, lattice-matched substrates are required for epitaxial growth of SL detectors. GaSb substrates are the most closely lattice matched to InAs/GaSb superlattice and thus were commonly used; however, the GaSb substrates commercially available at this time often suffered from high defect density, poor surface morphology, limited size, and high cost. Due to this fact, GaAs substrates, which have better quality and commercially available in large sizes, were evaluated for the growth of SL detectors (Bennett, 1998), demonstrating very promising results when complaint GaAs substrates were used (Brown *et al.*, 2000).

In parallel with growth optimization, studies of SL material properties were performed and new characterization methods were evaluated. SL detectors were predicted to have Auger recombination rates lower than in MCT detectors (Grein *et al.*, 1992, 1995). Auger rates were measured in InAs/InGaSb SLS using pump-probe experiment involving free electrons and were found to be indeed much lower than in MCT at room temperature (Ciesla *et al.*, 1996). In another work, the Auger recombination coefficients in InAs/GaSb SL's were deduced from the optical and electrical measurements that revealed a temperature behavior different from the bulk-like Auger process (Mohseni *et al.*, 1998b).

Several important studies were performed to evaluate basic SL properties. From spectrally resolved measurements of the infrared photodiode responsivity in applied magnetic fields, reduced effective masses and anisotropy of magnetic field–induced widening of the band gap were observed (Fuchs *et al.*, 1998b). Magnetotransport and photoluminescence measurements of superlattices grown at different substrate temperatures showed a transition from residual *n*-type to residual *p*-type doping with increasing growth temperature. It was found that a decrease in the electron concentration led to a strong increase in the PL intensity for *n*-type samples when the PL intensity of *p*-type samples was only weakly dependent on the hole concentration. These dissimilarities in PL characteristics were attributed to the difference in electron and hole transport and scattering mechanisms (Bürkle *et al.*, 2000). The minority electron diffusion lengths in $n^+ - p$ InAs/GaSb superlattice photodiode with cutoff wavelength at 7.7 μm were measured from 5.3 to 100 K using temperature-dependent EBIC technique, and the electron lifetime was obtained (Li *et al.*, 2004). In addition, new characterization methods, such as spectral ellipsometry, were successfully used for spectroscopic assessment of composition and structural quality of InAs/GaInSb SL (Wagner *et al.*, 1998).

In 1996, Johnson *et al.* (1996) demonstrated a double heterojunction InAs/GaInSb SLS photodiode operating at 77 K with dark current density of $I_d = 0.08$ A/cm^2 and responsivity of 0.8 A/W at 9 μm. At the same time, Fuchs and colleagues at Fraunhofer IAF in Freiburg started on a series of work that significantly advanced the performance of MWIR and LWIR SL detectors (Fuchs *et al.*, 1998a, 1997a; Walther *et al.*, 2005a; Yang *et al.*, 2002) and led to the demonstration of the first 256 × 256 focal plane array (FPA). At T = 77K, the FPA showed a cutoff wavelength of 5 μm, quantum efficiencies of 30%, detectivity values exceeding 10^{13} Jones, and a noise equivalent temperature difference (NETD) of 11.1 mK for an integration time of 5 ms and f/2 optics (Walther *et al.*, 2005b). Other significant works from the Fraunhofer Group included the analysis of dark current mechanisms in SL detectors (Yang *et al.*, 2002), the study of surface leakage, and passivation development (Fuchs *et al.*, 1998a; Rehm *et al.*, 2005).

Another major contribution to LWIR SL detector development during this time frame came from Professor Razeghi's group at the Northwestern University. Their work resulted in the demonstration of InAs/GaSb superlattice photodiodes with a cutoff wavelength around 7 μm at 77 K and the dark current density of about 10^{-5} A/cm^2 in devices with sulfide-based passivation (Mohseni and Razeghi, 2001; Mohseni *et al.*, 2001, 1999, 2000; Wei *et al.*, 2005). Researchers at Northwestern University, the U.S. Naval Research Laboratory, and U.S. Air Force Research Laboratory also made important progress in the development of very long-wavelength infrared (VLWIR) SL detectors operating in the spectral range 15–32 μm (Aifer *et al.*, 2003; Hood *et al.*, 2005b; Mohseni *et al.*, 2001; Wei *et al.*, 2002a,b).

2.4. Recent development

Research and development effort from 2006 to 2010 centered on two key areas. In device development, the emphasis has been on detectors based on heterostructure designs to reduce dark current and increase quantum efficiency (QE). There has also been a large investment in FPA development, with emphasis on improving fabrication processes to attain high uniformity and repeatability. The interest in the technology grew significantly during this period, involving more research teams including those from industry.

Heterojunction-based detector designs were shown to be highly effective in improving detector characteristics. Broadly speaking, they are either based on the nBn (Maimon and Wicks, 2006), pBp (Maimon, 2010), or XBn (Klipstein, 2008) design or variations of the double heterojunction (DH) design. The first category includes the single-band superlattice nBn detector (Rodriguez *et al.*, 2007), the dual-band superlattice nBn detector (Khoshakhlagh *et al.*, 2007), the superlattice pMp detector (Nguyen *et al.*, 2009a), and the superlattice pBn detector (Hood *et al.*, 2010a). The second category includes the superlattice DH structure (Delaunay *et al.*, 2007a; Vurgaftman *et al.*, 2006), the p-π-M-n detector (Nguyen *et al.*, 2007b), the PbIbN structure (Gautam *et al.*, 2010), and the complementary barrier infrared detector (CBIRD; Ting *et al.*, 2009a). Superlattices with complex supercells were also incorporated in heterojunction designs, either as barriers or as absorbers. These include the "W" (Aifer *et al.*, 2010b, 2006, 2005, 2010a; Canedy *et al.*, 2007; Kim *et al.*, 2007; Vurgaftman *et al.*, 2006) and the "M" (Nguyen *et al.*, 2009a, 2008b, 2007b, 2008a; Nguyen and Razeghi, 2007a) superlattices. A more detailed description of these designs is given in Section 4.

There has been continuous effort to improve material quality by optimizing growth parameters. Studies of doping levels, growth temperature, interfacial layer thicknesses, and material strain demonstrated the effect

of these parameters on device performance (Canedy *et al.*, 2010; Haugan *et al.*, 2010; Hoffman *et al.*, 2007, 2008; Khoshakhlagh *et al.*, 2009). Although there has been constant improvement in the quality, size, and availability of commercially available GaSb substrates, the requirements have become even more stringent for FPA fabrications. As an alternative to SL growth on GaSb substrates, very promising results of SL growth on GaAs substrates have been demonstrated (Abdollahi Pour *et al.*, 2009; Das *et al.*, 2008; Nguyen *et al.*, 2009c).

With the general improvement in device dark current density, the side wall surface leakage currents have become more noticeable. Surface leakage current reduction in fully pixelated devices has become a topic of interest. The surface leakage current depends on the etching process parameters, postetch cleaning, and surface passivation. The need for high-quality sidewalls led to the development of effective pixel isolation technique using dry etching with inductively coupled plasma (ICP) systems as reported by groups from the Northwestern Univeristy (NWU; Huang *et al.*, 2009), the Jet Propulsion Laboratory (JPL; Nguyen *et al.*, 2010a), and the University of New Mexico (UNM; Tan *et al.*, 2010). Many passivation methods have been explored. These include side wall treatment with ammonium sulfide (Hood *et al.*, 2005a), AlGaAsSb regrowth (Rehm *et al.*, 2005), deposition of SiO_2 (Herrera *et al.*, 2008; Hood *et al.*, 2005b), polyimide (Hood *et al.*, 2007), and SU-8 (Kim *et al.*, 2009). A shallow-etch mesa isolation (SEMI) technique (Aifer *et al.*, 2007) has also been developed for leakage current reduction.

Following the first 256×256 SL FPA demonstration in 2005, Fraunhofer IAF and NWU demonstrated 288×384 (Walther *et al.*, 2007) and 320×256 (Delaunay *et al.*, 2007b) FPAs in 2007. Fraunhofer's array showed good NETD values of 27.9 mK at the cutoff wavelength of 4.9 μm, whereas NWU's array showed a longer cutoff of 12 μm with NEDT of 340 mK. In the same year, JPL and Raytheon Vision Systems (RVS) demonstrated their first 256×256 p-i-n detector-based FPA with 10.5 μm cutoff wavelength (Rhiger *et al.*, 2007). In 2008, UNM demonstrated a 256×256 MWIR FPA based on a type-II InAs/GaSb superlattice detector with an nBn design (Kim *et al.*, 2008). Also in 2008, NWU fabricated a 320×256 FPA with 10 μm cutoff wavelength using a double heterostructure (DH) design to minimize the surface leakage (Delaunay *et al.*, 2008); this resulted in an improvement in the NETD value to 33 mK. In 2009 NWU developed an 320×256 FPA from their recently introduced M-structure (Delaunay *et al.*, 2009). This array demonstrated similar QE as previous FPAs, but a dark current level that was seven times lower. In the same year, JPL and RVS demonstrated the capabilities for larger format FPA fabrication with a $1\text{k} \times 1\text{k}$ FPA with 4 μm cutoff. A 640×512 LWIR FPA based on heterostructure designs was demonstrated (Hill *et al.*, 2009b) by JPL. RVS and

JPL have also demonstrated CBIRD-based 256 × 256 LWIR FPA (Rhiger *et al.*, 2010).

In 2010, Teledyne and HRL joined in FPA development. Teledyne utilized the graded gap "W" hybrid SL design in a 256 × 256 FPA with a 9.4 μm cutoff (Hood *et al.*, 2010b), while HRL used the barrier heterostructure design for a 320 × 256 FPA with a 9.0-μm cutoff (Terterian *et al.*, 2010). During this same year, the largest LWIR SL FPA was fabricated by both NWU and JPL with 1k × 1 k format (Gunapala *et al.*, 2010; Manurkar *et al.*, 2010), and these achievements can be contributed to the improvement in FPA manufacturing processes (Delaunay *et al.*, 2007c; Nguyen *et al.*, 2010b). In efforts to find a solution to the cost and limitation issues with GaSb substrates, NWU demonstrated a 320 × 256 MWIR FPA based on the p-i-n detector design and a 320 × 256 LWIR FPA based on the p-π-M-n design (Razeghi *et al.*, 2010), both grown on GaAs substrates. The successful demonstration of type-II superlattice FPAs on alternative substrates makes the technology promising for third-generation imaging.

3. BASIC PROPERTIES OF TYPE-II SUPERLATTICES

In this section, we explore the basic properties of the type-II InAs/Ga(In)Sb superlattices that distinguish them from bulk infrared material and describe how these properties lead to tunneling suppression and Auger reduction, and how they affect carrier transport. We begin with a brief overview of the antimonide material system from which the type-II superlattices are constructed.

3.1. The 6.1 Å material system

Table 1.1 lists some basic properties of common families of semiconductors used for making infrared photodetectors. All have diamond or zincblende crystal structures. In general, as we move from the covalent group IV semiconductors on the left side of the table to the more ionic II–VI semiconductors on the right, the lattice constant becomes larger, the chemical bond becomes weaker, and the material becomes softer as reflected in the values of the bulk modulus. The materials toward the left of the table are more mechanically robust, which leads to better manufacturability, as is evident in the dominance of silicon and GaAs among electronic/optoelectronic semiconductor materials. On the other hand, the semiconductors on the right side of the table tend to have smaller direct band gaps, which enable strong, bulk band-to-band absorption, leading to high quantum efficiency mid-wave infrared (MWIR) and long-wave infrared (LWIR) detectors such as those based on InSb and HgCdTe (MCT).

TABLE 1.1 Selected properties of common families of semiconductors used in mid-wave and long-wave infrared photodetectors

	Si	Ge	GaAs	AlAs	InP	InGaAs	AlInAs	InAs	GaSb	AlSb	InSb	HgTe	CdTe
Group	IV	IV	III-V	III-V	III-V	III-V	III-V	III-V	III-V	III-V	III-V	II-VI	II-VI
Lattice Constant [Å]	5.431	5.658	5.653	5.661	5.870	5.870	5.870	6.058	6.096	6.136	6.479	6.453	6.476
Bulk Modulus [GPa]	98	75	75	74	71	69	66	58	56	55	47	43	42
Direct Gap [eV]	-	-	1.426	-	1.350	0.735	-	0.354	0.730	-	0.175	−0.141	1.475
MWIR/LWIR Detection Method	Heterojunction Internal photoemission (HIP)		Quantum well/dot Intersubband (QWIP/QDIP)		Quantum well Intersubband (QWIP)			Bulk (MW)/ Superlattice (MW/LW) Band-to-Band			Bulk B-B	Bulk Band-to-Band	

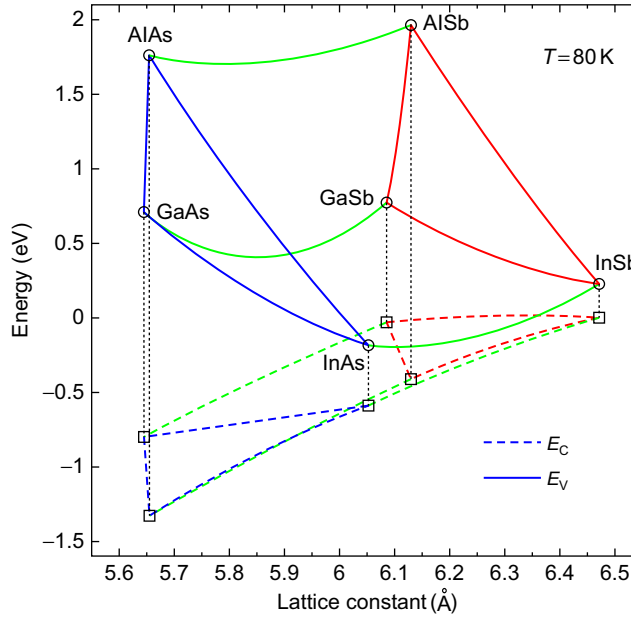

FIGURE 1.3 Zone center (Γ-point) conduction and valence band edge positions plotted against lattice parameter for antimonide, arsenide, and arsenide-antimonide III–V semiconductors.

Figure 1.3 shows the (Γ-point) conduction and valence band edge positions for antimonide, arsenide, and arsenide-antimonide group III–V semiconductors plotted against their lattice constants. The nearly lattice-matched semiconductors of InAs, GaSb, and AlSb are referred to as the 6.1 Å material system (Kroemer, 2004) since InAs, GaSb, and AlSb all have lattice constants of approximately 6.1 Å. They are also commonly referred to as the antimonides (InAs is included by virtue of being closely lattice-matched to GaSb and AlSb). As illustrated in Fig. 1.4, with the availability of type-I nested or straddling, type-II staggered, and type-II broken-gap (misaligned, or type III) band offsets among the GaSb/AlSb, InAs/AlSb, and InAs/GaSb material pairs, respectively; there is considerable flexibility in forming a rich variety of alloys and superlattices. Together with their alloys with InSb, GaAs, and AlAs, the 6.1 Å semiconductors provide a great degree of versatility. In particular, the overlap between the InAs conduction band and the GaSb valence band in the type-II broken gap alignment is unique among common semiconductor families and the so-called interband devices exploit this property specifically.

The 6.1 Å material system occupies an interesting position among the infrared semiconductor families listed in Table 1.1. Although it has

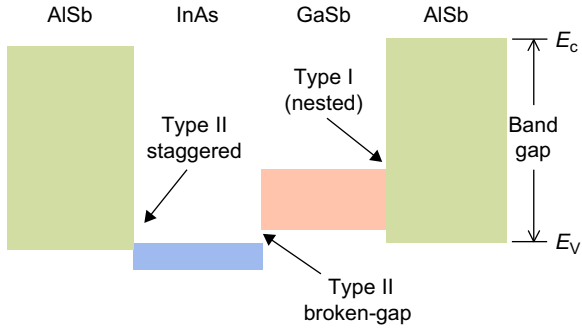

FIGURE 1.4 Schematic illustration of the energy band alignment in the nearly lattice-matched InAs/GaSb/AlSb material system. The shaded solid rectangles indicate the relative positions of the InAs, GaSb, and AlSb energy band gaps. Three types of band alignment are available in this material system: (1) type-I (nested) band alignment between GaSb and AlSb, (2) type-II staggered alignment between InAs and AlSb, and (3) type-II broken-gap alignment between InAs and GaSb.

intermediate material robustness, it is capable of strong, normal-incidence band-to-band absorption for high quantum efficiency, with bulk GaSb having a direct band gap in the short-wave infrared (SWIR), InAs in the MWIR, and InAs/Ga(In)Sb superlattices in the SWIR, MWIR, and LWIR. The valence-to-conduction band infrared absorption mechanism also avoids the operating-temperature-limiting phonon scattering problem encountered in detectors based on the intersubband absorption mechanism.

The antimonides can be epitaxially grown on GaSb or InAs substrates with very close lattice matching. In particular, 4-inch diameter GaSb substrates became commercially available in 2009. As their quality continue to improve, large diameter substrates offer economy of scale for focal plane array (FPA) fabrication, as well as the prospect for very large format arrays.

The antimonides are used in a wide variety of semiconductor devices. The InAs/GaAs/AlSb resonant interband tunneling diodes (RITD) exhibit very large peak-to-valley ratios at room temperature (Söderström *et al.*, 1989; Ting *et al.*, 1990). An InAs/AlSb resonant tunneling diode had demonstrated record-breaking oscillation frequency for a room temperature solid-state electronic oscillator in 1991 (Brown *et al.*, 1991). Antimonide-based high-electron mobility transistor (HEMT) and heterojunction bipolar transistor (HBT) showed high-frequency operation with much lower power consumption than GaAs- and InP-based devices (Bennett *et al.*, 2005). Antimonide-based devices are highly effective in

thermophotovoltaics (TPV) applications (Hitchcock *et al.*, 1999; Wang *et al.*, 1999). The antimonides are used for making state-of-the-art high-power solid-state infrared lasers in 2–3 μm range (Shterengas *et al.*, 2007). An antimonide-based mid-infrared interband cascade laser (Yang *et al.*, 2007) is employed in a tunable laser spectrometer for methane detection on the Mars Science Laboratory. The type-II interband heterostructure backward diode ("Schulman diode") is a highly sensitive detector essential for passive millimeter-wave imaging cameras (Moyer *et al.*, 2008; Schulman *et al.*, 2002). Asymmetric InAs/GaSb/AlSb resonant interband tunneling diodes have been proposed for use as nonmagnetic spin filters (Ting and Cartoixà, 2002, 2003), whereas asymmetric InAs/GaSb/AlSb quantum wells have been predicted to exhibit quantum spin Hall effect (Liu *et al.*, 2008). The application of the antimonides in MWIR/LWIR photodetectors is the focus of this work.

3.2. Tunneling suppression

In constructing superlattice-based infrared detector structures, special considerations should be given to the absorber superlattice intrinsic properties, many of which are revealed by band structure. We begin by examining the complex band structure of bulk InAs and GaSb in Fig. 1.5, calculated using an enhanced effective bond orbital model (Cartoixà *et al.*, 2003) that includes bulk inversion asymmetry effects. The material parameters

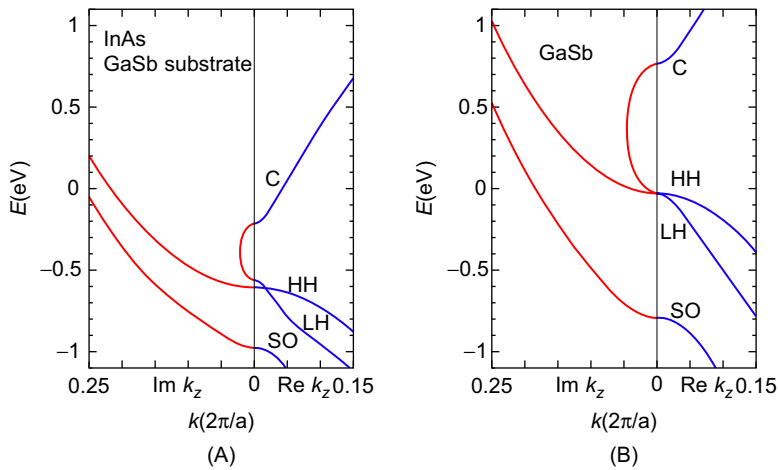

FIGURE 1.5 Complex band structure in the [001] direction for (A) InAs and (B) GaSb. In each graph, real wave vector is plotted in the right portion and imaginary wave vector in the left portion.

are taken from Vurgaftman *et al.* (2001). The complex band structure shows the conduction and valence bands, as well as the evanescent states. The evanescent states may be believed as "propagating" according to $\exp(-|k_z|z)$ or $\exp(ik_z z)$, where k_z is an imaginary quantity. Therefore, they are associated with imaginary wave vectors as shown in the left panels of Fig. 1.5A and B. The tunneling leakage property of an infrared photodiode is controlled by the characteristics of the evanescent waves in the band gap. At a given energy, if allowed by symmetry, the most favorable tunneling leakage path is provided by the evanescent state with the smallest imaginary wave vector. This is given by the branch of imaginary band connecting the conduction band edge to the light-hole band edge. This is seen clearly in Fig. 1.5A, where the InAs heavy-hole and light-hole bands are split slightly due to a small strain (we intentionally strained InAs to the GaSb substrate lattice constant). In general, the magnitude of the imaginary wave vector is larger in semiconductor with larger band gaps (specifically, the energy gap between the conduction band edge and the light-hole band edge) as can been seen by comparing the complex band structures of InAs and GaSb in Fig. 1.5. Alternatively, it can be said that larger conduction band effective mass also results in reduced tunneling since semiconductors with larger band gaps also have larger conduction band effective masses. The fact that small imaginary wave vector is associated with small band gap is the fundamental reason for the tunneling leakage problem encountered in LWIR homojunction pn diode based on narrow-gap bulk semiconductors.

We next examine a superlattice band structure to see how tunneling leakage is reduced in LWIR type-II superlattices. Figure 1.6 shows the band structure of a (22,6)-InAs/GaSb LWIR superlattice, calculated using an enhanced effective bond orbital model (Cartoixà *et al.*, 2003). The calculation does not include space charge effects (charge transfer from GaSb to InAs due to the broken-gap alignment), interface type, or interfacial diffusion, and it is subject to the limitations of the band structure model and uncertainties in the accuracy of material parameters. Therefore, as with other band structure calculations presented in this work, it should be treated only as semiquantitative when comparing with experimental results. A prominent feature of the superlattice band structure that distinguishes it from that of the typical bulk semiconductor is the splitting of the highest heavy-hole band (HH1) and the highest light-hole band (LH1) at the zone center. Although the infrared absorption edge is determined by the gap between the lowest conduction band (C1) and the HH1 band, the electron effective mass is determined by the C1-LH1 gap. In unstrained bulk semiconductors, the two gaps are the same. In the superlattice, the larger C1-LH1 gap leads to a substantially larger electron effective mass relative to that of a bulk semiconductor with the same fundamental band gap. The larger electron effective mass

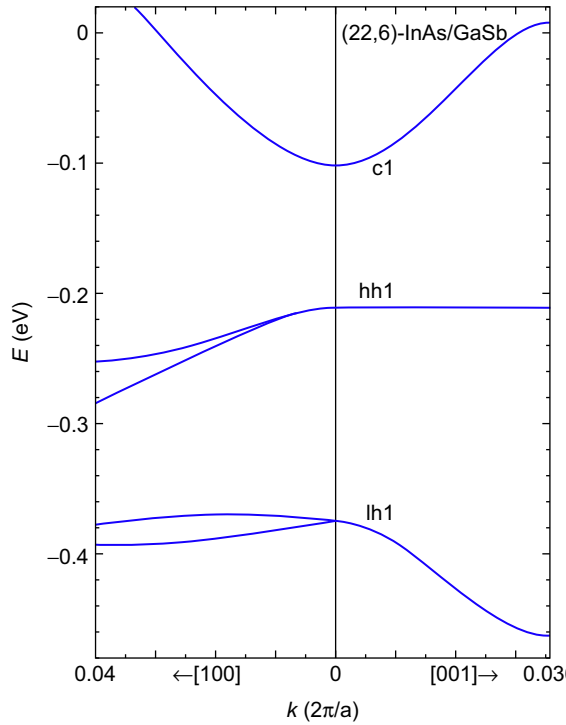

FIGURE 1.6 Band structure of a (22,6)-InAs/GaSb superlattice along the growth direction (right portion) and the in-plane direction (left portion).

is beneficial for reducing band-to-band tunneling, as well as trap-assisted tunneling.

3.3. Auger reduction

The splitting of the HH1 and LH1 bands can also result in the suppression of the Auger-7 recombination process, in which a minority electron recombines with a majority hole across the band gap while exciting another majority hole deeper into the valence bands. In the case of the (22,6)-InAs/GaSb superlattice shown in Fig. 1.6, because the HH1-LH1 separation is actually larger than the C1-HH1 separation, energy and momentum conservation considerations render it difficult to find matching HH1-LH1 transitions for C1-HH1 transitions, thereby suppressing Auger-7 events. Note that the degree to which a given type-II superlattice can benefit from Auger suppression depends on the details of the band structure and doping levels; the subject has been studied extensively by Grein and coworkers (Flatte and Grein, 2009; Grein and Ehrenreich, 1997; Grein *et al.*, 2002, 1992, 1995).

3.4. Effective masses and transport

Another prominent feature of the band structure shown in Fig. 1.6 is that the HH1 band is nearly dispersionless along the growth direction. Both the dispersionless HH1 band structure and the increased electron effective mass contribute to a larger joint density of states (JDOS). This results in a larger absorption coefficient, which, to first order, is directly proportional to the JDOS. This helps to compensate for the small optimal matrix element disadvantage inherent in type-II superlattices.

The band structure in Fig. 1.6 reveals important information about carrier transport properties that can affect detector design. We note that the C1 band shows strong dispersion along both the growth (z) and an in-plane direction (x), whereas the HH1 band is highly anisotropic and appears nearly dispersionless along the growth (transport) direction. Therefore, we expect the electron and hole density of states to be 3D and 2D, respectively. The calculated conduction and valence subband zone center effective masses along the x (in-plane) and z (transport) directions are as follows: $m_{\mathrm{c}}^{\mathrm{x}}* = 0.023\,m_0$ and $m_{\mathrm{c}}^{\mathrm{z}}* = 0.022\,m_0$, and $m_{\mathrm{hh1}}^{\mathrm{x}}* = 0.04\,m_0$ and $m_{\mathrm{hh1}}^{\mathrm{z}}* = 1055\,m_0$. It is interesting to note that the electron effective mass along the growth direction is quite small (even slightly smaller than in-plane electron effective mass), and the superlattice conduction band structure near the zone center is approximately isotropic. This is in stark contrast to the highly anisotropic valence band structure. Recalling that carrier group velocity is given by $\mathbf{v} = \nabla_{\mathbf{k}} E(\mathbf{k})/\hbar$, where $E(\mathbf{k})$ describes the band structure, we would expect very low hole mobility and diffusivity along the growth direction. Therefore, for this LWIR superlattice absorber, detector designs based on hole transport would be unfavorable. The fact that holes have more difficulty diffusing along the growth direction toward the collecting contact than diffusing laterally can be problematic in a focal plane array (FPA). For an FPA with fully reticulated pixels (physically isolated pixels, defined by etching), lateral diffusion transports the minority carriers to the pixel sidewalls, where surface recombination could take place readily in the absence of good surface passivation. In a planar-processed FPA with nonreticulated pixels, strong lateral diffusion means that minority carriers can spread easily to neighboring pixels, resulting in image blurring.

To understand the physical origin for the near isotropy in the conduction band and the extreme anisotropy of the valence band, we compare the band structure of the (22,6)-InAs/GaSb superlattice (Fig. 1.6) with that of the (6,34)-InAs/GaSb superlattice shown in Fig. 1.7. The calculated effective masses for the (6,34)-InAs/GaSb superlattice are as follows: $m_{\mathrm{c}}^{\mathrm{x}}* = 0.173\,m_0$ and $m_{\mathrm{c}}^{\mathrm{z}}* = 0.179\,m_0$, and $m_{\mathrm{hh1}}^{\mathrm{x}}* = 0.062\,m_0$ and $m_{\mathrm{hh1}}^{\mathrm{z}}* = 6.8\,m_0$. Figure 1.8 shows the schematic energy band diagrams for both superlattices, along with the positions of the C1, HH1, and LH1 states relative to

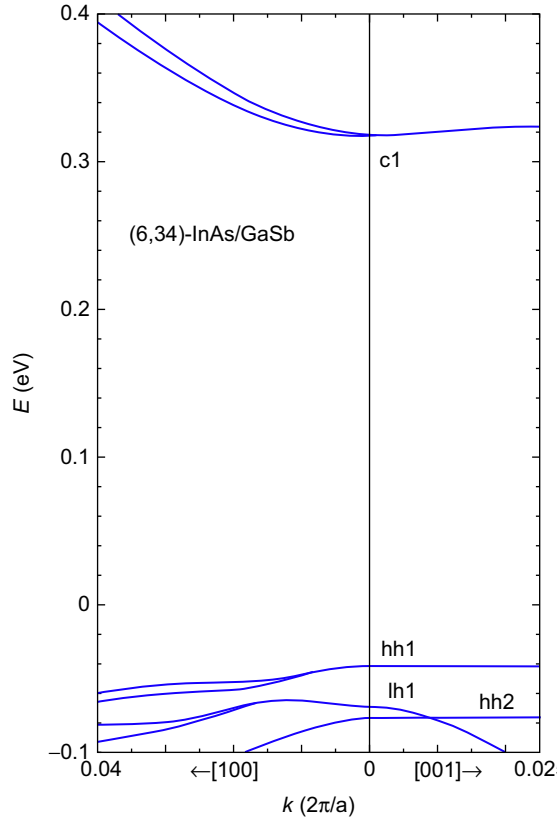

FIGURE 1.7 Band structure of a (6,34)-InAs/GaSb superlattice along the growth direction (right portion) and the in-plane direction (left portion).

the InAs and GaSb band gaps. Figure 1.8A shows that the C1 level of the (22,6)-InAs/GaSb superlattice is in the broken gap region. Therefore, an electron in the C1 level can travel along the growth direction without having to tunnel through any forbidden band gap regions. This explains the low electron effective mass in the growth direction. If we decrease the InAs quantum well width and push the C1 level into the GaSb band gap, as in the case of the (6,34) superlattice shown in Fig. 1.8B, the growth direction electron effective mass then becomes considerably larger. It is interesting that the in-plane electron effective mass in the (6,34) superlattice has also become nearly as large; this is mainly due to nonparabolicity in the bulk InAs conduction band.

Returning to the (22,6)-InAs/GaSb superlattice, we note in Fig. 1.8A that the HH1 level is also in the broken gap region. Then why is the HH1 effective mass so large along the growth direction? The reason is that the

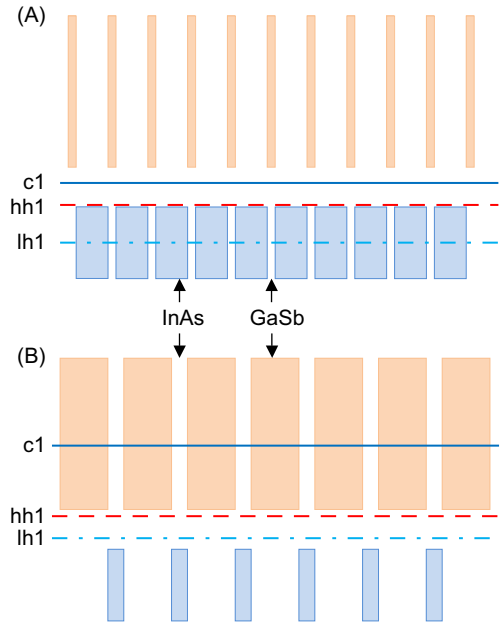

FIGURE 1.8 Schematic energy band diagrams of (A) (22,6)-InAs/GaSb superlattice and (B) (6,34)-InAs/GaSb superlattice, along with the c1, hh1, and lh1 energy levels. The energy band gaps of InAs and GaSb are indicated by shaded solid rectangles.

symmetry of the heavy-hole states. In the C1 level, the quantized level in the InAs conduction band quantum well can couple with the propagating light-hole states in the GaSb layers. For the HH1 level, by symmetry, the quantized heavy-hole states in the GaSb quantum well cannot couple to the propagating conduction band states in InAs despite having the same energy and instead has to couple with evanescent states with large wave vectors in InAs. As a result, the quantized heavy-hole states in neighboring GaSb quantum wells are essentially isolated from one another, leading to the dispersionless HH1 band.

Hole mobility along the growth direction may be quite acceptable in some superlattice structures. Figure 1.9 shows the detailed HH1 band structure for a (14,7)-InAs/GaSb superlattice and a (8,6)-InAs/GaSb superlattice, which are used in LWIR and MWIR detector structures, respectively. We note that the dispersion of the MWIR superlattice is much stronger than the LWIR superlattice; the MWIR HH1 effective mass is ~20 times smaller than that for the LWIR superlattice. Even for the LWIR superlattice, a closer look at the HH1 band structure reveals that the hole velocity may not be as low as first appeared. Figure 1.9A shows that in

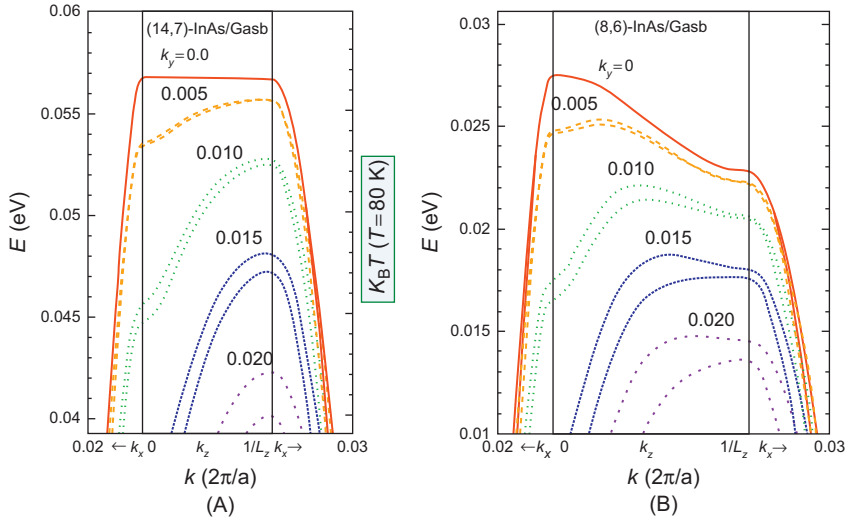

FIGURE 1.9 The heavy-hole 1 subband band structure of the (14,7)-InAs/GaSb superlattice in Graph (A) and the (8,6)-InAs/GaSb superlattice in Graph (B). In each graph, the central panel shows band structure along the growth direction (k_z) from the reduce zone center to the zone boundary. The side panels show the continuation of the band structure plotted along the in-plane direction k_x. The HH1 bands for several k_y values are plotted. In each graph, L_z is the number of monolayers in each period of the superlattice. A vertical bar inserted between the two graphs indicates the size of k_BT (6.9 meV for $T = 80$ K) on the energy scale; the top of the bar coincides with the HH1 valence band edges of the two superlattices.

the LWIR superlattice, for $k_y = 0$, the HH1 band has very little dispersion along k_z (z being the growth direction), with maximum occurring at the center of the reduced Brillouin zone. But as the result of interaction with other subbands, the HH1 band dispersion along the growth direction becomes appreciably larger as the in-plane momentum (k_y) increases; the band maximum along the k_z direction quickly switches from the reduced zone center to the zone boundary. At lower temperatures, we expect holes to occupy the less dispersion portions of the HH1 band, for which the hole density of states (DOS) is more like 2D and hole velocities along the growth direction are low. At higher temperatures, we expect the more dispersive parts of the HH1 to be occupied also. The thermalized holes would occupy the part of the DOS that is more 3D-like, and would attain higher velocities. Figure 1.9B shows the corresponding HH1 band structure plot for the (8,6)-InAs/GaSb MWIR superlattice. Note that in this case, the HH1 band shows a reasonable amount of dispersion even at $k_y = 0$ and its hole

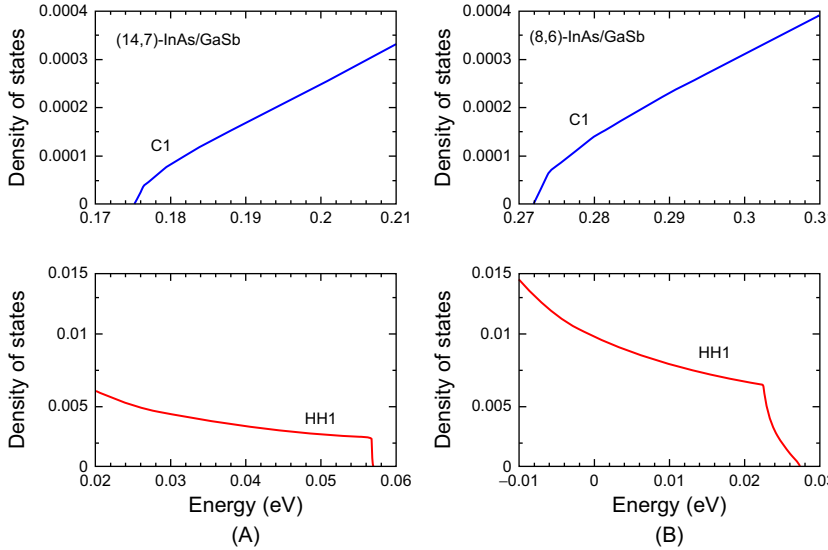

FIGURE 1.10 Conduction and valence band edge density of states (DOS) for the (14,7)-InAs/GaSb superlattice in Graph (A) and the (8,6)-InAs/GaSb superlattice in Graph (B). The portions of conduction and valence band DOS shown originate from the C1 and HH1 subbands, respectively.

transport properties should be much better than that of the LWIR superlattice. Nevertheless, even for the MWIR superlattice, the dispersion along the in-plane directions are much larger (see the side panels of Fig. 1.9B), thus favoring lateral hole diffusion. This is an issue that should be considered when choosing an n-doped type-II superlattice as an infrared absorber.

Figure 1.10 shows the actual calculated density of states for the (14,7)-InAs/GaSb LWIR superlattice and the (8,6)-InAs/GaSb MWIR superlattice. The conduction band DOS resembles the standard 3D DOS $\left(\propto \sqrt{E - E_c}\right)$ though with distinct differences due to band nonparabolicity. The HH1 DOS differs qualitatively from both the standard 3D and the 2D (step-like) DOS. The form of the DOS can affect our understanding of device performance. A standard tool used to study detector characteristics is dark current analysis, in which we fit experimentally measured dark current to analytical forms for various dark current sources (diffusion, generation-recombination, tunneling). This allows us to extract information on the dark current–generating mechanisms and carrier lifetimes (Pellegrino and DeWames, 2009; Rhiger *et al.*, 2009). In the typical dark current analysis, the carrier densities are modeled using the standard 3D DOS appropriate for bulk semiconductors. But as shown in Fig. 1.10,

superlattice DOS (specifically VB DOS) can be quite different from bulk DOS. This can affect the accuracy of dark current analysis. We note that there is tentative indirect evidence from LWIR superlattice infrared detector dark current analysis that the hole density switches from 2D to 3D with increasing temperature (Nguyen *et al.*, 2009b).

4. SUPERLATTICE INFRARED DETECTORS

The key to achieving high-performance infrared detection is in attaining high quantum efficiency and low dark current. With the ability to grow thick layers of high-quality superlattices with low defect density, resulting in sufficiently high absorption coefficient and large diffusion length, high quantum efficiency is now readily achievable. The typical dark current mechanisms include tunneling leakage, Auger processes, Shockley-Read-Hall (SRH) processes, and surface leakage. In the previous section we discussed how the band structure of appropriately designed superlattices leads to tunneling reduction and Auger suppression. In this section, we discuss how unipolar barriers are used to reduce dark currents associated with SRH processes and surface leakage.

4.1. Unipolar barriers

The use of heterostructures to improve HgCdTe (MCT) infrared detector performance is a well-established practice (Arias *et al.*, 1991; Pultz *et al.*, 1991; Tung *et al.*, 1992). Detector structures such as the double-layer heterojunction (DLHJ) have demonstrated significant advantages over their homojunction counterparts. The use of heterostructures is also prevalent in group III–V semiconductor-based infrared detectors. A particularly useful heterostructure construct is the unipolar barrier. The term "unipolar barrier" was introduced recently to describe a barrier that can block one carrier type (electron or hole) and allows the unimpeded flow of the other (Ting *et al.*, 2009b,a) as illustrated in Fig. 1.11. The concept of the unipolar barriers existed long before they were called as such. The double-heterostructure (DH) laser, which makes use of a pair of complementary unipolar barriers, was first described in 1963 (Alferov and Kazarinov, 1963; Kroemer, 1963), soon after the concept of heterostructure devices. Unipolar barriers have also been used extensively to enhance infrared detector performance. White (1987) used unipolar barriers to block the flow of majority carrier dark current in photoconductors without impeding minority carriers. A DH detector design can be used to reduce diffusion dark current emanating from the diffusion wings surrounding the absorber layer (Carras *et al.*, 2005). The nBn (Maimon and Wicks, 2003, 2006; Pedrazzani *et al.*, 2008) or XBn (Klin *et al.*, 2009; Klipstein, 2005, 2008;

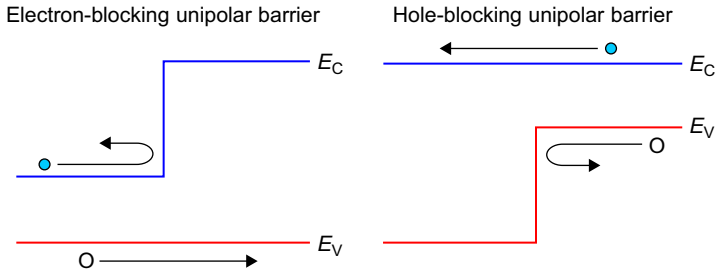

FIGURE 1.11 Schematic illustration of the energy and diagrams of an electron- and a hole-blocking unipolar barriers.

Klipstein *et al.*, 2010) detector structure uses a unipolar barrier to suppress dark current associated with Shockley-Read-Hall processes without impeding photocurrent flow, as well as to suppress surface leakage current (Pedrazzani *et al.*, 2008). In general, unipolar barriers can be used to implement the barrier infrared detector architecture for increasing the collection efficiency of photogenerated carriers (by deflecting them towards the collector, in the same way a back-surface field layer functions in a solar cell structure) and reducing dark current generation without inhibiting photocurrent flow.

4.2. Dark current reduction using unipolar barriers

We illustrate the use of unipolar barriers for dark current reduction by comparing diodes based on homojunction and heterojunction designs. One of the key uses for the unipolar barrier is in the suppression of generation-recombination (G-R) dark current due to SRH processes. As discussed by Klipstein (2008), in a conventional photodiode, there exists a threshold temperature T_0, above which the dark current is diffusion limited and below which G-R limited. In a homojunction pn diode, the G-R current is proportional to $\exp(-E_g/2kT)$ (assuming mid-gap defect level) and is predominantly generated in the depletion region. If the depletion region of the pn diode is replaced by a larger gap semiconductor (a barrier), in which the $\exp(-E_g/2kT)$ factor is greatly reduced (particularly at lower temperatures), the SRH dark current generation can be virtually eliminated. The suppression of the G-R dark current allows the detector to operate at higher temperature or with higher sensitivity.

It is important that the G-R reducing barrier does not block the photocurrent. In a p on n structure, this can be accomplished by inserting an electron-blocking unipolar barrier at the junction of the pn diode to form the pBn diode (Klipstein, 2008). Figure 1.12 shows the reverse bias energy

band diagrams of a pn diode and a pBn diode, calculated using heterojunction drift-diffusion simulation (Daniel *et al.*, 2000). Both structures use an *n*-type MWIR InAs/GaSb superlattice as the absorber. The doping levels in the p and n regions are taken to be $p = 1 \times 10^{16}\,\mathrm{cm}^{-3}$ and $n = 1 \times 10^{16}\,\mathrm{cm}^{-3}$, respectively. The pBn structure contains an undoped 2000 Å wide electron-blocking unipolar barrier made from a GaSb/AlSb superlattice. The bottom panel of Fig. 1.12 shows the calculated magnitudes of the SRH recombination rates given by the expression $r_{\mathrm{SRH}} = (\mathrm{np} - \mathrm{n_i^2})/[\tau_{\mathrm{p}}(\mathrm{n} + \mathrm{n_i}) + \tau_{\mathrm{n}}(\mathrm{p} + \mathrm{p_i})]$. A value of $\tau_{\mathrm{p}} = \tau_{\mathrm{n}} = 100\,\mathrm{ns}$ (Donetsky *et al.*, 2010) is used in the simulation. For the pn junction, the calculated peak SRH recombination rate in the middle of the depletion region is approximately five orders of magnitude larger than the baseline rate outside the depletion region. In the pBn structure, the calculated SRH recombination rate is greatly reduced.

We next examine the suppression of G-R dark current in a *p*-type LWIR detector using a hole-blocking unipolar barrier. We consider a homojunction np diode and a heterojunction NIp diode, both with *p*-type 10-μm LWIR InAs/GaSb superlattice as the absorber. The reverse bias energy band diagrams for the two devices are shown in Fig. 1.13, along with the calculated magnitudes of the SRH recombination rates. The doping densities in the p and n regions of the homojunction diode are taken to be $p = 1 \times 10^{16}\,\mathrm{cm}^{-3}$ and $n = 1 \times 10^{16}\,\mathrm{cm}^{-3}$, respectively. The NIp structure uses an InAs/AlSb superlattice as the wide-gap "N" and "I" region, which acts as a hole-blocking unipolar barrier to the LWSL superlattice absorber. In the NIp structure, the 3000 Å segment of the barrier adjacent to the *p*-type absorber (doped to $p = 1 \times 10^{16}\,\mathrm{cm}^{-3}$) is undoped, whereas the remaining portion of the wide-gap region is doped to $n = 1 \times 10^{16}\,\mathrm{cm}^{-3}$. A value of $\tau_{\mathrm{p}} = \tau_{\mathrm{n}} = 35\,\mathrm{ns}$ (Connelly *et al.*, 2010; Donetsky *et al.*, 2010; Pellegrino and DeWames, 2009) is used in the simulation. For the superlattice homojunction np diode, the calculated peak SRH recombination rate in the middle of the depletion region is approximately three orders of magnitude larger than the baseline rate outside the depletion region. In the NIp structure, the calculated SRH recombination rate is again greatly reduced. Note that in the NIp structure, as well as in the pBn structure discussed above, photogenerated minority carriers in the absorber region can flow towards the collector without being impeded. The use of the unipolar barrier can suppress SRH-related dark current without reducing photoresponse.

The pBn and the NIp structures described above are actually quite similar. If we took an nBp structure (the complement of the pBn structure, with a hole-blocking unipolar barrier) and replaced the "n" contact layer with a wider gap "N" layer (which would not affect device performance, so long as we could make ohmic contact to the "N" layer), then we end up with the NIp structure (the "B" barrier layer is now called

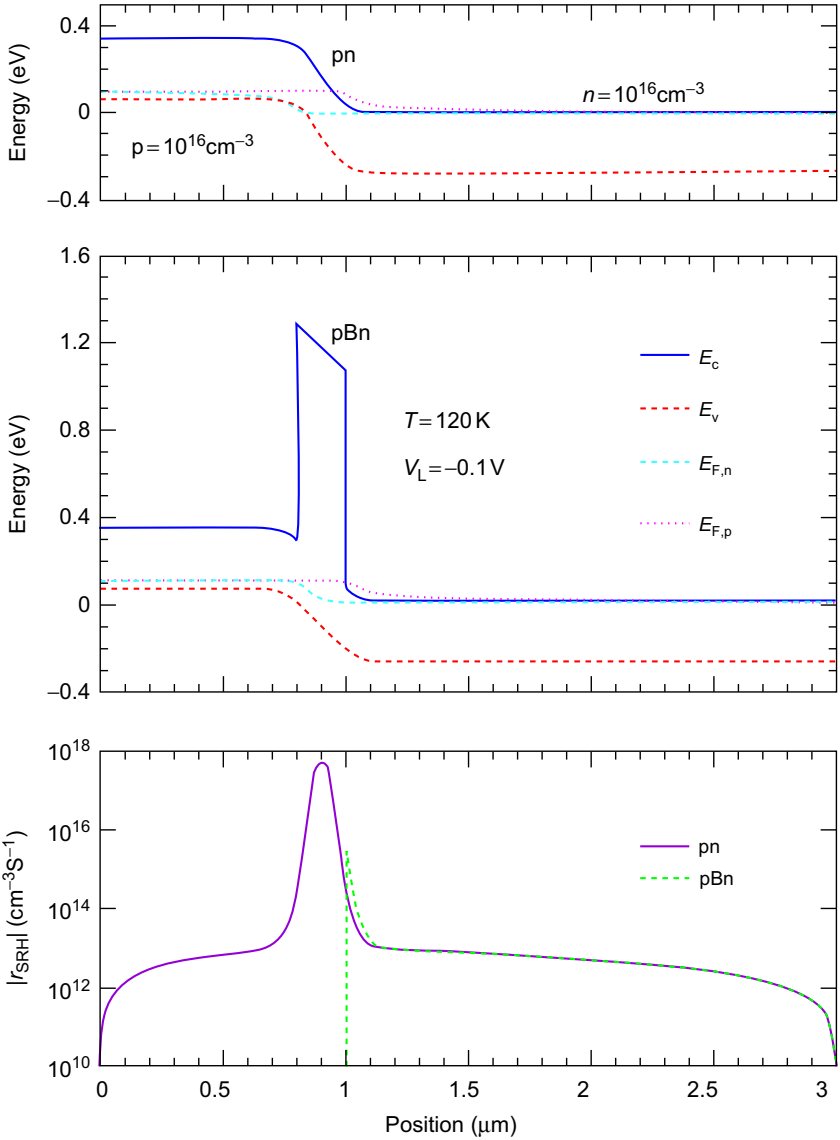

FIGURE 1.12 The top and middle panels show the calculated 80 K reverse-bias energy diagrams along with quasi Fermi levels for a mid-wavelength infrared superlattice pn junction diode and a pBn diode, respectively. The bottom panel shows the calculated magnitude of the Shockley-Read-Hall recombination rates for the two structures as functions of position.

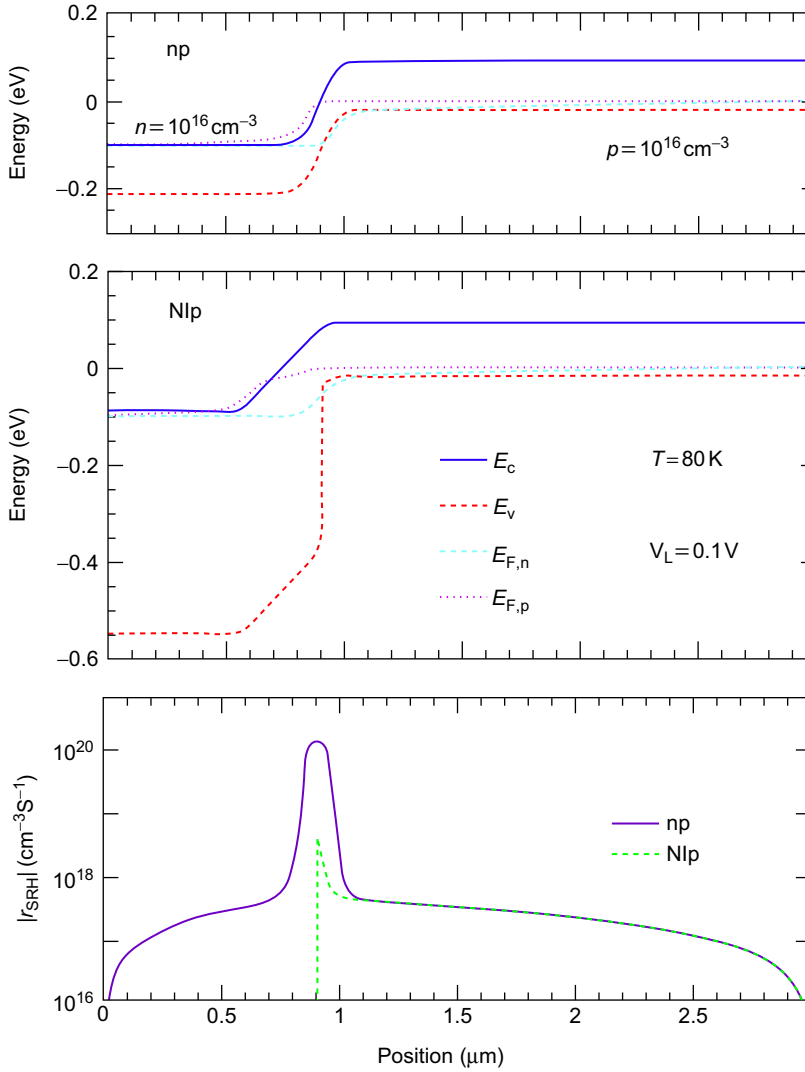

FIGURE 1.13 The top and middle panels show the calculated 80 K reverse-bias energy diagrams along with quasi Fermi levels for a long-wavelength infrared superlattice np junction diode and a NIp diode, respectively. The bottom panel shows the calculated magnitude of the Shockley-Read-Hall recombination rates for the two structures as functions of position.

the "I" layer). Calculations on the nBn structure also show similar SRH recombination rate suppression (Ting *et al.*, 2010). In all cases, a majority carrier blocking unipolar barrier is used for G-R dark current suppression, without blocking minority carrier photocurrent.

Unipolar barriers can also be used to suppress surface leakage current. Wicks and coworkers demonstrated experimentally that by introducing a judiciously placed unipolar barrier into an *n*-type InAs photoconductor or an InAs pn photodiode, forming an nBn detector or a unipolar barrier photodiode, the surface leakage current can be substantially reduced (Savich *et al.*, 2010; Wicks *et al.*, 2010). Although these demonstrations were done using InAs photodetectors, which are known to suffer from surface leakage, the operating principles should apply equally well to superlattice-based photodetectors.

4.3. Building unipolar barriers

In general, unipolar barriers are not always readily attainable for the desired infrared absorber material as both the absorber and barrier materials require (near) lattice matching to available substrates, and the proper band offsets must exist between the absorber and the barrier. The practical realization of the MWIR nBn detectors (Maimon and Wicks, 2006) is enabled only by the fortuitous existence of the approximate valence band alignment between the $InAs_{0.91}Sb_{0.09}$ absorber and AlSbAs electron-blocking barriers, both can be epitaxially grown on GaSb substrate. (Alternatively, InAs absorber and AlSbAs barrier can be grown on an InAs substrate.) As described by Carras *et al.* (2005), finding a hole-blocking unipolar barrier for $InAs_{0.91}Sb_{0.09}$ is challenging and considerable effort was required to circumvent such difficulties. Building unipolar barriers for InAs/GaSb superlattices is relatively straightforward because of the flexibility of the 6.1 Å materials afforded by the three different types of band alignments among InAs, GaSb, and AlSb.

For electron-blocking unipolar barriers to InAs/GaSb superlattices, we note that for superlattices with the same GaSb layer widths, their valence band edges tend to line up fairly closely. This is because the large heavy-hole mass makes the HH1 energy level relatively insensitive to the well width. Therefore, an electron-blocking unipolar barrier for a given InAs/GaSb superlattice can be formed by using either another InAs/GaSb with thinner InAs layers (Nguyen *et al.*, 2008a; Ting *et al.*, 2009a) or a GaSb/AlSb superlattice (all with approximately the same GaSb layer widths to ensure valence band alignment).

For hole-blocking unipolar barriers to InAs/GaSb superlattices, there are many options as illustrated in Fig. 1.14. Superlattices with complex supercells, such as the four-layer InAs/GaInSb/InAs/AlGaInSb "W" structure (Aifer *et al.*, 2006, 2010a; Canedy *et al.*, 2007; Kim *et al.*, 2007; Vurgaftman *et al.*, 2006) or the four-layer GaSb/InAs/GaSb/AlSb "M" structure (Nguyen *et al.*, 2009a, 2008b, 2007b, 2008a; Nguyen and Razeghi, 2007a), have been used as hole-blocking unipolar barriers. Alternatively,

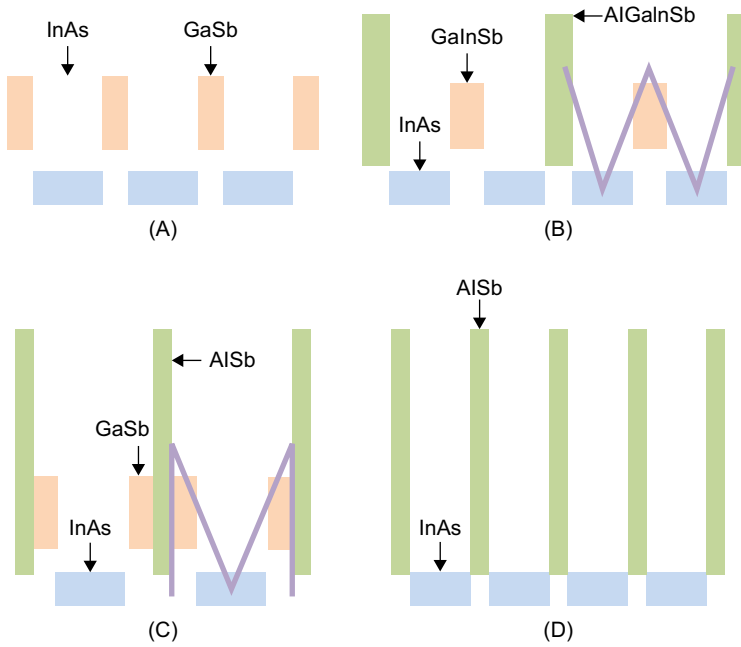

FIGURE 1.14 Schematic energy band diagrams of (A) an InAs/GaSb superlattice, (B) an InAs/GaSb/InAs/AlSb "W" superlattice, (C) an InAs/GaSb/AlSb/GaSb "M" superlattice, and (D) an InAs/AlSb superlattice.

the two-layer InAs/AlSb superlattice (Fig. 1.14D) has also served well (Ting *et al.*, 2009a). Incidentally, both the conduction band edge and the valence band edge of the "W" superlattice (WSL) can be adjusted. As a result of this flexibility, the WSL has been used as a hole-blocking unipolar barrier, an absorber, as well as an electron-blocking unipolar barrier.

Figure 1.15 illustrates another aspect of the usefulness of the unipolar barrier. Figure 1.15A shows the calculated energy band diagram of a LWIR superlattice detector based on an earlier double heterostructure design similar to the one described by Johnson *et al.* (1996). In this structure, p-GaSb and n-GaSb are used as electron and hole barriers to the LWIR absorber superlattice. Because the band edges of GaSb does not line up with those of the absorber, there are energy spikes that can block photocurrent. Figure 1.15B shows a more recent double heterostructure design that incorporates unipolar barriers. The LWIR InAs/GaSb absorber SL is surrounded by an electron-blocking unipolar barrier made from an MWIR InAs/GaSb superlattice and a hole-blocking unipolar barrier made from an InAs/AlSb superlattice. The spikes are no longer present, and photocurrent can flow unimpeded.

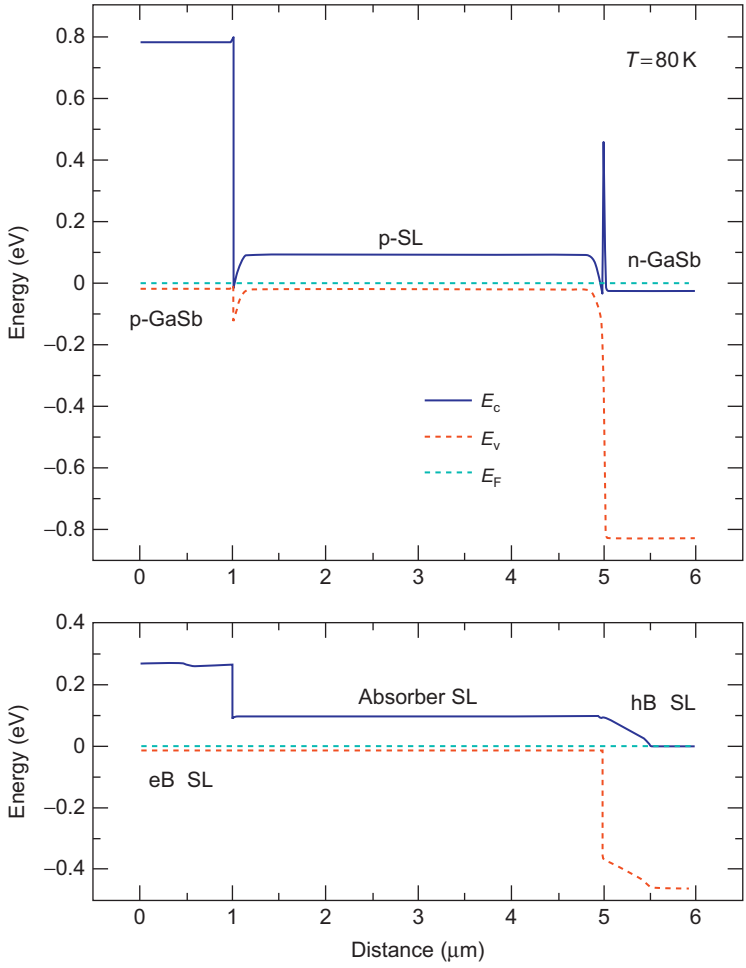

FIGURE 1.15 The top panel shows the energy band diagram of double heterostructure (DH) consisting of a InAs/GaSb superlattice absorber surrounded by p-GaSb and n-GaSb barriers. The bottom panel shows the energy band diagram of DH with the superlattice absorber surrounded by a pair of electron- and hole-blocking unipolar barriers.

4.4. Barrier infrared detector

The type-II broken-gap InAs/Ga(In)Sb superlattice can be used as mid- or long-wavelength infrared absorber. As discussed earlier, superlattices or alloys built from the InAs/GaSb/AlSb material system can also be custom-designed to build matching unipolar barriers to the infrared absorber

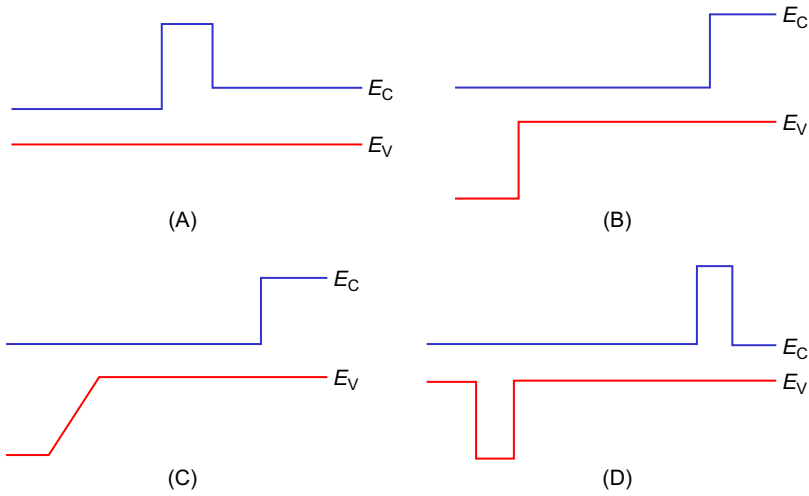

FIGURE 1.16 Schematic flat-band energy band diagrams of (A) a double heterostructure (DH), (B) a dual-band nBn structure, (C) a DH with a graded-gap junction, and (D) a complementary barrier structure.

superlattice. In particular, the ability to tune the positions of the conduction and valence band edges independently in a type-II superlattice is especially helpful in the design of unipolar barriers. Figure 1.16 illustrates the energy band diagrams of some idealized examples of the type-II superlattice-based infrared detectors that make use of unipolar barriers. Broadly speaking, they are based on either the nBn/pBp/XBn architecture (Klipstein, 2008; Maimon, 2010; Maimon and Wicks, 2003, 2006) or the variations of the double heterostructure design.

Figure 1.16A illustrates a dual-band superlattice nBn detector (Khoshakhlagh *et al.*, 2007) in which an LWIR superlattice and an MWIR superlattice are separated by an AlGaSb unipolar barrier. This follows an earlier single-band superlattice nBn detector with an MWIR absorber and an AlGaSb barrier (Rodriguez *et al.*, 2007). The advantage of this type of architecture is simplicity (which often leads to better manufacturability) and the ability to suppress G-R and (electron) surface leakage dark current (Maimon and Wicks, 2006; Pedrazzani *et al.*, 2008; Wicks *et al.*, 2010). The concerns for the nBn architecture, when used with an n-doped type-II superlattice absorbers, are possible low hole mobility (particularly in LWIR structures) and strong lateral diffusion (Plis *et al.*, 2008). A variation of the superlattice nBn detector, in which the *n*-type contact layer is replaced by a *p*-type contact and thus forming the pBn structure, has also been reported (Hood *et al.*, 2010a).

Figure 1.16B illustrates a double heterostructure (DH) detector structure. The DH design is commonly used in laser structures and has been used in MWIR detectors with bulk semiconductor absorbers (Carras *et al.*, 2005; Reverchon *et al.*, 2004). Johnson *et al.* (1996) used a DH structure similar to the one shown in Fig. 1.15A, in which an LWIR superlattice is surrounded by barriers made from p-GaSb and n-GaSb. A more recent design consists of an LWIR InAs/GaSb absorber superlattice surrounded by an electron-blocking unipolar barrier made from an MWIR InAs/GaSb superlattice and a hole-blocking unipolar barrier made from an InAs/GaSb/AlSb/GaSb ("M") superlattice (Nguyen *et al.*, 2008b, 2007b, 2008a).

Figure 1.16C illustrates a variation of the double heterostructure (DH) detector structure, in which a graded gap region is inserted between the absorber and the hole barrier to reduce tunneling and G-R dark currents (Vurgaftman *et al.*, 2006). The structure is also used to enable the shallow-etch mesa isolation (SEMI) structure for surface leakage current reduction (Aifer *et al.*, 2010a). The design is very flexible. The hole-blocking unipolar barrier is typically made from a four-layer InAs/GaInSb/InAs/AlGaInSb "W" superlattice (WSL), although an InAs/AlInSb superlattice has also been used. The graded gap region is typically made from multiple segments of WSLs with progressively changing band gaps. The absorber has been made from a WSL or an InAs/GaInSb superlattice. The electron-blocking unipolar barrier has been made from WSL or p-GaSb.

Figure 1.16D illustrates another variation of the double heterostructure (DH) detector structure, called a complementary barrier structure (Ting *et al.*, 2009c), or a PbIbN structure (Gautam *et al.*, 2010). This is basically a DH structure surrounded by additional narrow-gap contact layers. The narrow-gap layers can be useful in the case in which it is difficult to make ohmic contact to the wide-gap barrier layers. In the PbIbN structure (Gautam *et al.*, 2010), all the layers are made from InAs/GaSb superlattices with different layer widths.

Yet another variation on the DH structure is the complementary barrier infrared detector (CBIRD) structure (Ting *et al.*, 2009a) illustrated in Fig. 1.17. The CBIRD design consists of a lightly p-doped InAs/GaSb absorber SL sandwiched between an n-doped InAs/AlSb hole-barrier (hB) SL, and a wider gap InAs/GaSb electron-barrier (eB) SL. The hB SL and the eB SL are designed to have approximately zero conduction and valence subband offset with respect to the absorber SL, that is, they act as a pair of complementary unipolar barriers with respect to the absorber SL. A heavily doped *n*-type InAsSb region adjacent to the eB SL acts as the bottom contact layer. The unipolar-barrier-based Np junction between the hB SL and the absorber SL acts to reduce SRH-related dark current. The wider gap hB SL also serves to reduce trap-assisted tunneling. The eB SL serves

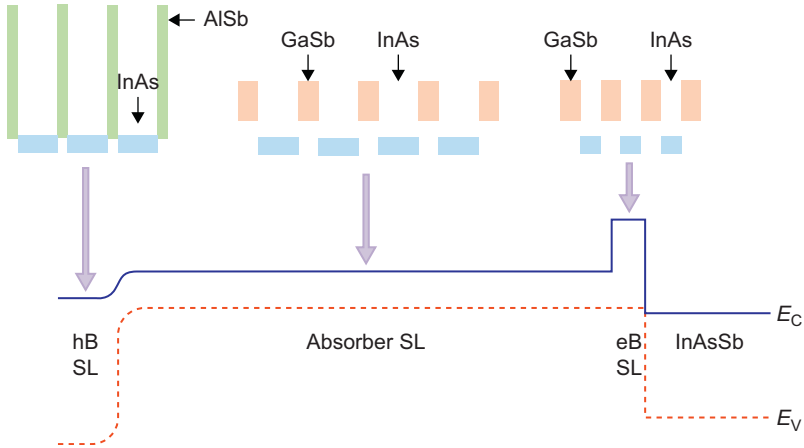

FIGURE 1.17 Schematic energy band diagram of a complementary barrier infrared detector (CBIRD) structure, in which a long-wave infrared InAs/GaSb superlattice absorber is surrounded by a InAs/AlSb superlattice hole-blocking unipolar barrier and a shorter period InAs/GaSb superlattice electron-blocking unipolar barrier.

to deflect photogenerated electrons toward the Np junction for collection (similar to back surface field in solar cells). Although the InAsSb layer also appears to provide a hole barrier on the left, the broken-gap band alignment between the eB SL and InAsSb facilitates interband tunneling and interface recombination, which reduces hole accumulation in the absorber region. In addition, the eB SL presents a taller barrier against extra electron injection from the bottom contact. Detailed results on this particular CBIRD device have been reported earlier (Ting *et al.*, 2009a, 2010).

Figure 1.18 shows the dark current–voltage characteristics of a CBIRD device compared to a homojunction device made with nominally the same absorber superlattice. The two detectors have approximately the same photoresponse, but the CBIRD shows a substantial dark current reduction over the homojunction superlattice detector. In general, the use of heterostructures, particularly unipolar barriers, has been highly effective in dark current reduction in type-II superlattice-based LWIR detectors. Figure 1.19 shows a compilation by D. R. Rhiger of the 78 K dark current densities plotted against detector cutoff wavelengths for homojunction and heterojunction type-II superlattice detectors reported in the literature since late 2010. In general, the devices with the lowest dark current densities are heterojunction devices. Furthermore, the dark current densities of several heterojunction devices reported by different institutions (Canedy *et al.*, 2009; Nguyen *et al.*, 2009a, 2010b) are approaching the levels calculated using the empirical "Rule 07" model (Tennant, 2010; Tennant

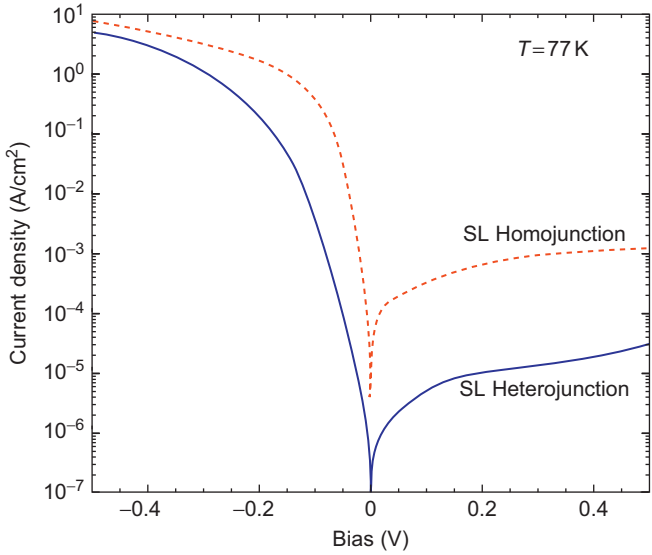

FIGURE 1.18 Dark current densities for a superlattice homojunction long wavelength infrared (LWIR) detector and a superlattice heterojunction LWIR detector taken at 77 K.

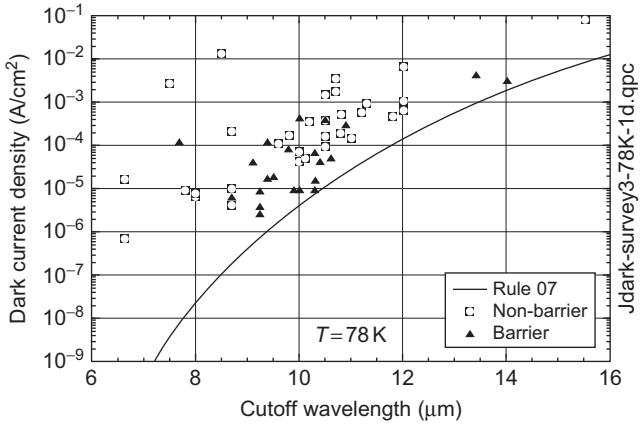

FIGURE 1.19 The 78 K dark current densities plotted against cutoff wavelength for type-II superlattice detectors reported in the literature since late 2010. The open and solid symbols indicate homojunction and heterojunction devices, respectively. The solid line indicates the dark current density levels calculated using the empirical "Rule 07" model. (Courtesy by D. R. Rhiger.)

et al., 2008), which provides a heuristic predictor of the state-of-the-art MCT photodiode performance.

Finally, we note that there is another type of antimonide superlattice infrared detector called the interband cascade infrared photodetector (ICIP), which is based on a radically different design (Li *et al.*, 2005; Yang *et al.*, 2010b,a). In its original incarnation (Li *et al.*, 2005), it was simply an interband cascade laser (ICL) diode structure (Yang, 1995) running in "reverse operation" as a photodetector. The operation of the ICIP is similar to that of the quantum cascade detector (Gendron *et al.*, 2004), except that since it is based on interband than intersubband transitions, it is capable of normal incidence infrared absorption. The operating principle of the ICIP is described in detail by Yang *et al.* (2010b).

5. DETECTOR FABRICATION AND CHARACTERIZATION

In order to evaluate the superlattice material and the detector structures described in the earlier sections, different structural, optical, and electrical characterization tools are used (Bürkle and Fuchs, 2002; Fuchs *et al.*, 1997b). In this section, we will focus on a few of these characterization techniques, including optical characterization, lifetime measurements, and noise measurements. We will also describe one of the biggest challenges faced during fabrication of superlattice detectors, namely, the etching and passivation of the detector surfaces and how this affects the dark current and noise properties.

5.1. Detector fabrication

Surface leakage is a major challenge in the fabrication of InAs/GaSb superlattice-based detectors and arrays. High surface leakage current prevents full operation of the detector due to the high $1/f$ noise or can lead to excess charging of the ROIC and cause saturation. This requires the ROIC to have a larger electron capacity or high diode impedances in order to maximize full potential of the camera system.

One source of surface leakage comes for the presence of a nonzero surface potential. A nonzero surface potential at the sidewall interface leads to band bending, resulting in a high flat band voltage. If the overall surface potential is positive (negative), then the electron energy is decreased (increased) and the bands must bend downward (upward). The resulting accumulation/inversion of majority carriers can create conductive leakage pathways parallel to the sidewalls (Fuchs *et al.*, 1998a). For LWIR detector structures, especially with cutoff wavelengths longer than 10 μm, the amount of band bending becomes comparable to the band gap of

the device (Herrera *et al.*, 2008), so achieving near flat band condition is essential for high performance. One source of nonzero surface potential is the improper termination of the crystalline lattice at the semiconductor–air interface. Tetrahedral GaSb, InAs, and AlSb lattice is abruptly terminated at the surface during etching and leaves one or two dangling crystal bonds per surface atom. These dangling bonds can act as reaction sites for chemical reactions or surface states for electronic processes. Dangling bonds that are empty can contribute to the reduction in free energy and the lowering of the surface band profile, or they can be satisfied through adsorption of water, oxygen, etch byproducts, contaminants, or foreign atoms.

Surface states are another source of leakage current. The typical surface states are interfacial traps that come from attachment of etch byproducts, contaminants, or foreign atoms to the dangling bonds. These traps can be charged via interaction with the conduction and/or valence band of the semiconductor and capturing or emitting electrons or holes. Acceptor interface traps are negative when filled and neutral when empty, and donor interface traps are neutral when filled and positive when empty. If a large number of surface states are positioned within the band gap of the semiconductor, pinning of the Fermi level will occur. This can lead to a number of different undesirable effects, such as increased trap-assisted tunneling dark current, minority carriers drifting to the surface, and contribute to high surface recombination velocity, loss of quantum efficiency, or the creation of excess leakage current.

The problem with high surface leakage can begin with the quality of the etched sidewalls. It is important that unwanted contaminants, etch byproducts, or foreign atoms do not attach to the dangling bonds, leading to a change in the resistance at the surface. For the InAs/GaSb superlattice, the presence of a native oxide can form secondary compounds on the sidewall surface (such as In_2O_3 or Ga_2O_3) that acts as a good conductor and decrease the surface resistance. Good sidewall profile and high fill factor are highly desirable characteristics, especially for large format focal plane arrays with small pixels. Chemical wet etch is advantageous due to the minimal amount of sidewall damage; however, this becomes an unacceptable option due to the large degree of undercut and concave sidewall profiles. High-density plasma etching can alleviate this issue with its anisotropy due to the plasma sheath and ionized gas directionality, but poses challenges of its own. One challenge is plasma-induced damage, which has been found to leave etch residues and ripple patterns in the sidewalls (Kutty *et al.*, 2010; Nguyen *et al.*, 2009c; Rehm *et al.*, 2006). Another challenge with etching group III–V materials is preferential etching, where preferential loss of group V elements can create ripples along the sidewalls. The rough morphologies of the ripples become an additional source for electrical active sites. With a clean surface that is smooth and free

from unwanted contaminants, the challenge for passivation is alleviated, and any encapsulation that occurs during passivation can preserve the high-quality state of the sidewall surface.

Surface passivation is as important as the etching mechanism since it affects the electrical performance by satisfying dangling bonds with atoms that can modify the surface potential and possibly counteract any charges on the surface. It is important that the passivation technique does not etch the surface or roughen the surface. Further, the material needs to be non-conductive and does not contribute to the surface resistance. It can be seen that the resistance-area product has a linear relationship with the surface resistivity as given by the relation

$$\frac{1}{\mathrm{RA}} = \frac{1}{(\mathrm{RA})_{\mathrm{bulk}}} + \frac{1}{r_{\mathrm{surface}}}\frac{P}{A},$$

where $(\mathrm{RA})_{\mathrm{bulk}}$ is the resistance-area product of the bulk material, r_{surface} is the surface resistivity, P is the perimeter of the diode, and A is the area of the diode.

In addition to protecting the surface from chemical reactions, passivation can physically protect the surface from degradation and ensure stability of the device. Any passivation that encapsulates the surface can provide physical protection and also acts as a barrier to prevent diffusion of unwanted reactive species. This may be beneficial for subsequent steps in the FPA fabrication process such as epoxy underfill.

5.2. Optical characterization of superlattices

During the development of superlattice detectors, several different optical and optoelectronic characterization techniques have been used to study InAs/Ga(In)Sb superlattices. Photoluminescence (PL), absorption, and electroluminescence (EL) spectroscopy are all very useful tools for extracting information about the material quality, energy-level structure, dopant levels, etc. of these superlattices.

PL spectroscopy is a nondestructive characterization technique that provides information about the band structure, dopants, and trap energy levels. It is a well-established technique widely used to study material properties of bulk semiconductors, as well as of quantum structures (Lacroix *et al.*, 1996; Pavesi and Guzzi, 1994). This technique has also shown to be a powerful tool when studying the optical performance of superlattices. Information about the material quality is obtained from the PL intensity (Bürkle *et al.*, 2000; Canedy *et al.*, 2003; Haugan *et al.*, 2008; Schmitz *et al.*, 1995) and the width of the PL peak (Canedy *et al.*, 2003; Haugan *et al.*, 2006; Ongstad *et al.*, 2000). By studying the influence of

temperature and excitation power density on the PL peak amplitude and the peak position, respectively, other physical properties of the superlattice such as the recombination processes in the material and the variation of the band gap with temperature are revealed.

In EL charges are generated electrically rather than optically thus device fabrication is needed. This offers some additional degrees of freedom since specific regions of the detector structure can be studied separately. EL has been used as a tool to extract information about the material quality. In addition, it has served to explain some device characteristics in superlattice detectors. Rodriguez *et al.* (2005) observed a temperature dependence of the photoresponse for MWIR InAs/GaSb superlattices with activation energy of approximately 28 meV, which later was attributed to the activation energy of Be-dopants (Hoffman *et al.*, 2006), extracted with EL measurements. Furthermore, trap centers located in the band gap of a LW InAs/GaSb superlattice, observed by EL, contributed to the understanding of the dark current characteristics of those detectors (Yang *et al.*, 2002).

Absorption spectroscopy is a straightforward technique for extracting essential parameters about the detector performance, such as absorption quantum efficiency and spectral response. Very little sample preparation is required, which makes it a convenient way to extract quick feedback in the optimization process of the detector material (Höglund *et al.*, 2010). As described below, by combining absorption spectroscopy with the information gained from PL and EL, a good indication of the attainable performance of detectors fabricated from the studied material can be obtained.

Good IR detector material is characterized by high-absorption quantum efficiency (QE_a) and a long lifetime of the minority carriers (τ). Those properties are essential since the density of photon-generated carriers ($QE_a \Phi \tau / t$) need to be larger than the thermally generated carrier density for optimal performance of a detector fabricated from that material (Kinch, 2000; t is the thickness of the detector material and Φ is the photon flux). The absorption QE is easily attainable from transmission measurements (Höglund, 2010). By comparing the absorption QE with the external QE obtained by responsivity measurements, information about the transport properties in the material can be obtained. In Fig. 1.20, the spectra of the external QE and the absorption QE of a LW InAs/GaSb CBIRD detector are well correlated in terms of spectral distribution; however, the amplitude of the absorption QE is higher than the corresponding external QE. Since the absorption QE serves as an upper limit of the external QE (unless there is a gain in the structure), the difference between these QEs indicates that not all photogenerated carriers reach the contacts.

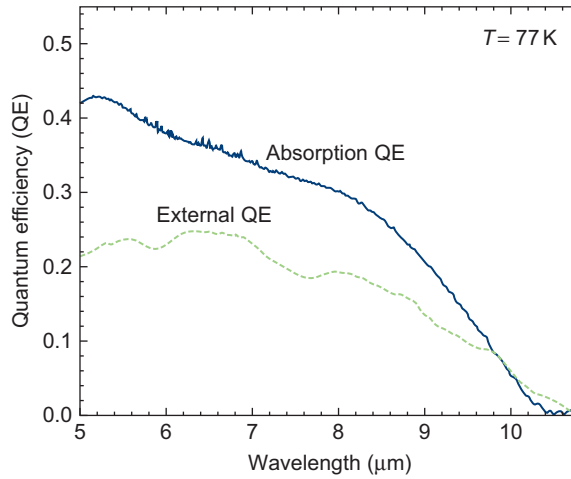

FIGURE 1.20 Absorption quantum efficiency versus external quantum efficiency in an InAs/GaSb CBIRD detector at an applied bias of 0.15 V.

To achieve a high collection efficiency of excited carriers the minority carrier lifetime should be long. The minority carrier lifetime is dependent on the radiative lifetime (τ_R), as well as the nonradiative lifetime (τ_{nR}). The nonradiative lifetime is influenced by several different recombination processes of which the most important ones are the Shockley-Read-Hall (SRH) recombination, Auger processes, and surface recombination. All of these processes add to the minority carrier lifetime according to the following equation: $\frac{1}{\tau} = \frac{1}{\tau_{Rad}} + \frac{1}{\tau_{SRH}} + \frac{1}{\tau_{Auger}} + \frac{1}{\tau_{surface}}$ (Ahrenkiel and Lundstrom, 1993). This equation illustrates that the recombination process with the shortest lifetime dominates the minority carrier lifetime. Different optical methods are used to extract the minority carrier lifetime in superlattice material (Connelly *et al.*, 2010; Donetsky *et al.*, 2010, 2009; Hoffman *et al.*, 2005), described in more detail in the next subsection. In order to distinguish which recombination process has the major influence on the minority carrier lifetime, PL and EL spectroscopy are used. When performing these studies, it is preferable to sandwich the absorber between two barriers to reduce the effect of surface recombination. (see suggestions by Ahrenkiel and Lundstrom, 1993). To get an understanding of the possible Auger-related processes that might limit the lifetime, the band structure of the material is studied. The band gap of the superlattice can be approximated by the peak energy of the PL (or EL) spectrum or with the cutoff wavelength of the absorption spectrum (Fig. 1.20). Some deviation

from the exact band gap energy is expected, depending on the temperature and on the excitation power that sets the excess carrier density in PL experiments. Bertru *et al.* (1999) observed a blueshift of the PL peak with increasing excess carrier density, varying as the third root of the excitation density. The blueshift was caused by filling of triangular wells formed at the InAs/GaSb interfaces. The triangular wells are induced by the Coulomb attraction between the separated holes and electrons located in the GaSb and the InAs layers, respectively. As with all semiconductors, the band gap of InAs/GaSb superlattices changes with temperature. In addition to this bandgap variation, the temperature change affects other processes that shift the PL peak position. For bulk material, a continuous redshift of the PL peak position with increasing temperature is observed. However, in a InAs/GaSb superlattice blueshift of the PL-peak with increasing temperature in the 2–125 K temperature range was observed by Bertru *et al.* (1999). The explanation given by this group was that the joint density of states of type-II quantum wells (QWs) differs from bulk and also from type-I QW structures. Band-to-band absorption behaves like $(\varepsilon - \varepsilon_0)^{1.5}$, which means that high k-value transitions will be favored. As the temperature is increased, the higher k-value states will be populated, which could cause the observed blueshift. These effects will cause minor errors in the estimation of the band gap, which should be considered when analyzing luminescence data.

Whereas the luminescence spectrum mainly probes the interband transitions between the lowest conduction band and the highest valence band (typically the heavy-hole band), absorption spectroscopy or Fourier transform PL excitation (PLE) could be used to study interband transitions between higher energy bands. To our knowledge, no PLE studies have been performed on InAs/GaSb superlattices so far. However, this technique has been successfully utilized to study higher energy transitions in other medium-infrared detector materials such as HgCdTe and InSb (Fuchs *et al.*, 1993); therefore, it could be a possible candidate for future studies of superlattice band structure. Several groups have used absorption spectroscopy to study interband transitions between higher energy levels in the superlattice. For example, excitonic peaks have been observed from interband transitions between the light-hole band and the conduction band and from the second heavy-hole band to the conduction band (Kaspi *et al.*, 2000; Rodriguez *et al.*, 2005). The energy subband separations obtained in these experiments can be used to identify the possible Auger processes in the material.

Near mid-gap energy levels are the main contributors to the SRH processes that limit the minority carrier lifetime. There were several attempts to measure these levels using optical techniques but so far they did not produce any conclusive results. However, indirectly the temperature

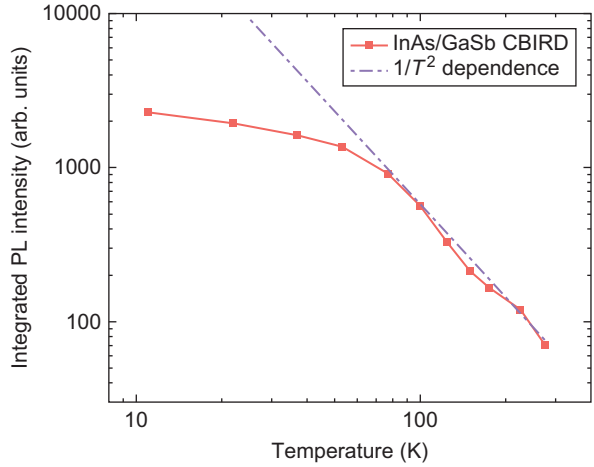

FIGURE 1.21 Temperature dependence of the integrated PL intensity of a LW InAs/GaSb CBIRD superlattice compared to the $1/T^2$ temperature dependence, which is characteristic for a material with SRH-limited minority carrier lifetime.

dependence of the luminescence intensity and the dependence of the luminescence intensity on excess carrier density indicate that such levels are present. The PL intensity is related to the nonradiative lifetime (τ_{nR}) according to the following: $\eta = \frac{I_{PL}^{(\infty)}}{\rho_0} = \frac{\tau_{nR}}{\tau_{nR}+\tau_R}$, where η is the internal QE, $I_{PL}(\infty)$ is the total number of emitted photons, ρ_0 is the total number of absorbed photons, and τ_R is the radiative lifetime (Ahrenkiel and Lundstrom, 1993). If $\tau_{nR} << \tau_R$, the PL intensity varies with temperature as τ_{nR}/τ_R. If the nonradiative processes are dominated by either Shockley-Read-Hall processes or Auger processes, τ_{nR}/τ_R varies proportionally to $1/T^2$ (Canedy *et al.*, 2003) or $1/T^{1.5}$ (Fuchs *et al.*, 2006). The experimentally observed PL intensity variation with temperature is plotted in Fig. 1.21 together with the theoretical $1/T^2$ dependence. This shows a strong correlation between the experimental data of the temperature dependence and the $1/T^2$ trend at temperatures higher than 77 K, which indicates that SRH processes limit the lifetime in this material. As the temperature is decreased below 77 K, the integrated PL intensity deviates from the $1/T^2$ temperature dependence and approaches a constant value. This is expected when the SRH lifetime and the radiative lifetime are comparable (Canedy *et al.*, 2003).

Further information about processes dominating the nonradiative lifetime can be obtained from the dependence of the EL intensity on the injected carrier density. Hoffman *et al.* (2005) and Fuchs *et al.* (2006) showed that for material in which Auger processes dominate the carrier lifetime,

the internal QE drops quickly with increasing excess carrier density, whereas the internal QE is almost independent of the excess carrier density when SRH processes dominate the lifetime.

By using calibrated measurement setups and comprehensive analysis of the results, quantitative information about the Auger coefficient and the minority carrier lifetime was obtained from studies of the temperature dependence of the EL intensity (Fuchs *et al.*, 2006; Hoffman *et al.*, 2005). The temperature dependence of the internal QE was correlated with the modeled QE for SRH-limited ($\mathrm{QE} \propto 1/T^2$) and Auger-limited ($\mathrm{QE} \propto 1/T^{1.5}$) minority carrier lifetime. When fitting the modeled QE to the measured QE, the Auger coefficient for a LWIR superlattice was extracted to be $10^{-24}\,\mathrm{cm}^6\,\mathrm{s}^{-1}$ and the minority carrier lifetime of a MWIR superlattice was deduced as a function of *p*-type background concentration. For a carrier background of $10^{15}\,\mathrm{cm}^{-3}$, the lifetime was deduced to be 100 ns, which is in reasonable agreement with the values measured by time-resolved PL spectroscopy for similar material (Donetsky *et al.*, 2009).

With the information obtained from absorption measurements and lifetime measurements, a good prediction of the fitness of the superlattice as an IR detector material can be obtained. The recombination processes limiting the lifetime are identified from variation of PL and EL intensities with temperature and excess carrier density. This information combined with the band structure of the superlattice is essential in the optimization process of the detector material and serves to improve the performance of the IR detectors.

5.3. Noise measurement

The detector performance is limited by the noise equivalent intensity (NEI) value that defines the minimal optical power the detector (or FPA) is capable of resolving for given optics and integration time. NEI gives the optical intensity that produces the electrical signal equivalent to the noise signal of the detector, so the lower noise of the detector, the lower optical flux it can detect. The noise power spectrum of a photovoltaic detector, S_{pv}, is given by $S_{\mathrm{pv}}(f) = S_{\mathrm{ph}} + S_{\mathrm{i}} + S_{\mathrm{e}}\,(f)$, where S_{ph}, S_{i}, and $S_{\mathrm{e}}\,(f)$ are the photon shot noise, the detector "fundamental" (shot and thermal), and detector excess noise, respectively. The photon shot noise is given by $S_{\mathrm{ph}} = 2\eta\Phi\mathrm{A}$, where η is the detector external quantum efficiency and Φ is the radiation flux density on the detector of area A. The detector "fundamental" noise is given by $S_{\mathrm{i}} = 2\mathrm{e}(I + 2I_0) = 2\mathrm{e}I + 4k_{\mathrm{B}}T/R_0$, where I and $I_0 = k_{\mathrm{B}}T/R_0$ are the diode current and the diode saturation current, respectively, T is the temperature, k_{B} is Boltzmann's constant, and R_0 is the differential resistance at zero bias (van der Ziel, 1970). The detector excess noise, which is very

often $1/f$ noise, can significantly degrade the detector performance and has to be minimized or preferably eliminated. The $1/f$ noise plays a significant role in MCT detectors, so significant research efforts were dedicated to understand the origin of the noise in these devices.

In the initial works, the noise spectra of the illuminated SL detector were studied and $1/f$ noise was not observed, yet the detector noise in these experiments was dominated by photon shot noise (Mohseni and Razeghi, 2001; Plis *et al.*, 2006). Recently, direct measurements of the noise spectra of high-performance SL heterodiodes based on a variant CBIRD design (Hill *et al.*, 2009a) were performed at different operational conditions to understand the effects of dark current and of the surface current on detector noise (Soibel *et al.*, 2010). These results demonstrated that intrinsically SL photodetectors do not exhibit $1/f$ noise. At the same time, these measurements clearly showed that sidewall leakage current not only increases the shot noise by contributing to higher dark current but more importantly it also introduces additional frequency dependent noise, resulting in much higher noise in the detector. Since strongly frequency-dependent noise can be generated by sidewall leakage current, it is important to fabricate high-performance SL detectors and focal plane arrays (FPAs) using a technology that minimizes the mesa sidewall leakage current. One way to achieve this is by the development of reliable sidewall passivation that can suppress the leakage current and prevent the onset of frequency-dependent noise. These results are described in more detail below and also in the reference (Soibel *et al.*, 2010).

The study focused on two representative devices designated as d1 and d2, which were fabricated simultaneously by wet etching from the same CBIRD wafer (Sb1593). These devices have very similar differential resistance-area product of $R_0A = 1200\,\text{ohm}\,\text{cm}^2$ (d1) and $R_0A = 1000\,\text{ohm}\,\text{cm}^2$ (d2) at $T = 77\,\text{K}$, but the dark current in device d2 is higher than in device d1 (Fig. 1.22). Based on measurement of dark current density dependence on device area/perimeter ratio, we attribute the higher dark current to detector mesa sidewall surface leakage current. The bottom panel of Fig. 1.23 shows the current noise, i_n, of the device d1 at several applied biases ranging from $V_\text{b} = 0\,\text{V}$ to $V_\text{b} = 0.4\,\text{V}$. The noise spectra are relatively flat from 1 Hz to 5 kHz, showing the absence of $1/f$ noise in this device. The shot noise in the device increases with an increase of the applied bias/current, as can be seen clearly from the noise spectral density at frequencies higher than 1 kHz; however, the general "flatness" of the noise spectra does not change with bias, and no onset of $1/f$ noise is observed. In contrast, the noise characteristics are profoundly different in the device d2 (Fig. 1.23, top). The noise amplitude is much larger than in device d1 and noise increases rapidly with the applied bias V_b; thus,

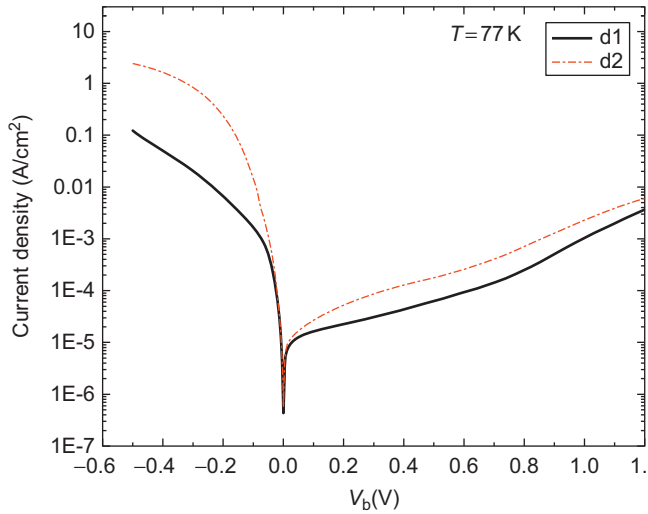

FIGURE 1.22 Current–voltage (I–V) characteristics of two CBIRD devices, d1 and d2, measured at $T = 77$ K.

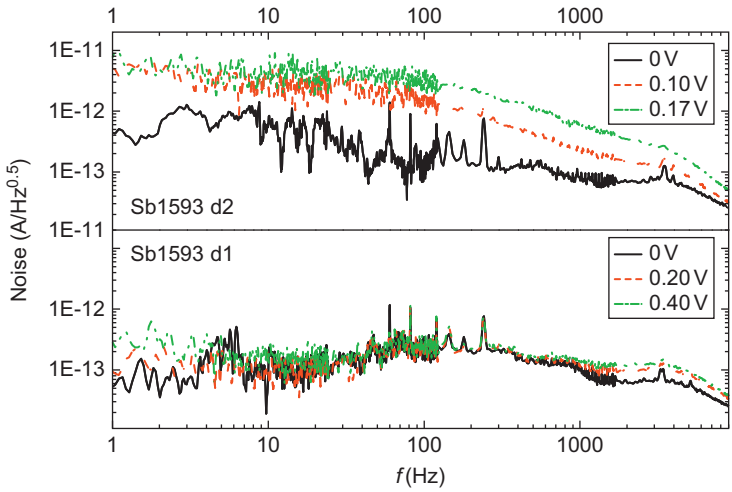

FIGURE 1.23 The current noise, i_n, versus frequency of the devices d1 and d2 at several applied bias voltages as indicated on the graph. The dark current in the device d2 is higher than in the device d1, and the higher dark current, which is attributed to detector mesa sidewall surface leakage current, results in large frequency-dependent noise. A small hump seen in the noise spectra near 100 Hz is attributed to the instrument noise since the hump size and shape is independent of detector bias.

the noise in this device is much higher than can be expected from a simple theoretical estimation of the shot noise. Moreover, the noise spectra are frequency dependent even at zero bias. At $V_b = 0.1$ V and $V_b = 0.17$ V, the noise spectra have a $1/f^{0.9}$ frequency dependence in the $f = 100$ Hz–4 kHz frequency range but become almost frequency independent at lower frequencies. The observed noise has frequency dependence similar to that of $1/f$ noise in the limited frequency interval of $f = 100$ Hz–4 kHz, and it becomes frequency independent at lower frequency. Such behavior is characteristic of flicker noise that is attributed to the surface states (van der Ziel, 1970). Indeed, the appearance of additional frequency noise associated with the surface states is consistent with the observation of surface leakage current that is also attributed to an electrical activity of the surface states. In particular, these noise measurements show that while intrinsic $1/f$ noise is absent in superlattice heterodiode, sidewall leakage current can become a source of strong frequency-dependent noise. This result underscores the importance of the development of reliable etching and sidewall passivation that can suppress the surface leakage current and prevent the onset of frequency-dependent noise.

There are additional sources of temporal noise in SL FPA such as the read-out noise, as well as the spatial noise, resulting from variations of the pixel characteristics across FPA. Recently, noise of the LWIR InAs/GaSb superlattices FPA with 9.6 μm cutoff wavelength was characterized at 80 K (Delaunay and Razeghi, 2009). This 320 × 256 array of 25 × 25 μm^2 detectors with a 30-μm pitch array was passivated with SiO_2 and hybridized to an ISC 9705 ROIC from Indigo Systems. The noise equivalent temperature difference in the array was found to be 23-mK for an integration time of 0.129 ms. The observed noise was described in terms of thermal, shot, read-out integrated circuit and photon noise. It was found that the FPA noise was dominated by the dark current shot noise or by the noise of the testing system at lower illuminations, whereas photon shot noise was the major noise source at photon fluxes higher than 1.8 $\times 10^{15}$ ph s^{-1} cm^{-2}. The $1/f$ noise was not observed in this FPA for frequencies above 4 mHz.

5.4. Lifetime measurement

The lifetime of minority carriers is a key parameter that defines both the dark current and quantum efficiency of photodetectors. Achievement of a long lifetime material is an important task for superlattice detector development that will advance the current state-of-the-art technology and will enable high-performance detectors and FPAs. The minority carrier lifetime in superlattices is set by both radiative and nonradiative (Auger and SRH) recombination processes, so it is essential for future material development to understand the contribution from each of these processes,

as well as the material and device design parameters affecting them. Several measurements of the minority carrier lifetime in superlattices were performed utilizing different techniques including photoconductivity measurements (Yang *et al.*, 2003), an electron beam–induced current technique (Li *et al.*, 2004), and time-resolved photoluminescence (Connelly *et al.*, 2010; Donetsky *et al.*, 2010, 2009), and by analyzing detector dark current (Pellegrino and DeWames, 2009).

In photoconductivity measurements, lifetime was determined from the change in the photoconductivity response with increase of the carrier density proportional to the laser excitation power (Yang *et al.*, 2003). Several LWIR detector samples with various doping densities were measured, and a lifetime decrease with temperature was observed, which was attributed to SRH recombination processes. The analysis of current versus voltage data of p-n + LWIR SL detector showed that generation-recombination currents dominate the dark current at modest reverse bias at 80 K, and by taking the energy of the dominant recombination centers to be located at the intrinsic Fermi level, the lowest minority carrier lifetime was determined to be 35 ns (Pellegrino and DeWames, 2009). This lifetime provides an excellent fit to the current–voltage characteristics of the detectors in the temperature range $T = 40-130$ K and explains the observed quantum efficiency. The minority carrier lifetimes in the absorbers of mid- and long-infrared SL detectors were measured by time-resolved photoluminescence using an optical modulation technique (Donetsky *et al.*, 2010, 2009). The measured lifetimes for mid- and long-infrared superlattices were 100 ns and 31 ns, respectively, which is much shorter than the lifetime of 1 μs in the MCT detector material that was studied in the same experiment. It was proposed that the short minority carrier lifetime in Sb-based material is a consequence of higher phonon energy, resulting in exponential increase of the electron capture cross-sections of nonradiative traps (Donetsky *et al.*, 2010). In another work, the lifetime was extracted from the exponential decay of the photoluminescence signal to be 30 ns at 77 K, dominated by SRH recombination processes (Connelly *et al.*, 2010). In addition, a radiative recombination constant of $1.8 \times 10^{-10}\,\mathrm{cm}^3/\mathrm{s}$, an upper limit of the Auger recombination coefficient of $10^{-28}\,\mathrm{cm}^6/\mathrm{s}$ at 60 K, and an acceptor level of ~20 meV above the valence band were determined.

These tests provide important information about lifetime and recombination mechanisms, and more work is currently underway to further understand factors affecting lifetime and the correlation between the lifetimes observed in the time-resolved PL experiments and dark current measurements. It is not clear at this point what sets the short lifetime in Sb-based SL and how to increase it to desirable values of several hundred nanoseconds (Pellegrino and DeWames, 2009). The influence of the shallow defect levels on the lifetime is another open question. The nonradiative

recombination process identified in PL measurements was attributed to the defects with energy located near valence band edge; however, these defects are not expected to provide a large contribution to generation-recombination current, which is typically associated with defects near middle of the band gap. Recently, a theory postulating existence of two trap levels in the band gap was proposed to explain these results, yet additional experimental and theoretical work is required to fully understand this phenomenon.

5.5. Lifetime and dark current

MWIR and LWIR superlattices (Connelly *et al.*, 2010; Donetsky *et al.*, 2010, 2009; Pellegrino and DeWames, 2009) studied so far found to have substantially short lifetimes compared with MCT (Edwall *et al.*, 1998; Kinch *et al.*, 2005). As described in the previous section, direct time-resolved photoluminescence measurements at 77 K yielded a lifetime of 100 ns for MWIR SL and ~30 ns (Donetsky *et al.*, 2010, 2009) for LWIR SL (Connelly *et al.*, 2010; Donetsky *et al.*, 2010), whereas indirect inference through dark current analysis of an LWSL SL yielded a lifetime of 35 ns (Pellegrino and DeWames, 2009). The question then arises as to why the observed dark current densities (as reflected in the RA_{eff} value) are not correspondingly worse for the superlattices. This turns out to be related to tunneling suppression in superlattices. Recall that the diffusion dark current density from the p-side of a pn diode is given by $J_{\text{diff}} = qn_{\text{i}}^2 L_{\text{N}}/(N_{\text{A}}\tau_n)$, where n_i is the intrinsic carrier density, L_N is the diffusion length (or absorber width), N_{A} is the acceptor dopant density, and τ_n is the minority carrier (electron) lifetime. In a typical LWIR superlattice, the doping density is on the order of $\text{p} = 1 - 2 \times 10^{16}\,\text{cm}^{-3}$, which is considerably higher than the doping level found in the LWIR MCT (typically low, $10^{15}\,\text{cm}^{-3}$). This is possible because of tunneling current suppression in superlattices. The higher doping compensates for the shorter lifetime, resulting in relatively low diffusion dark current. However, to achieve the true promise of superlattices with performance exceeding that of MCT requires the understanding of the origin of the relatively short carrier lifetimes found in the present generation of InAs/GaSb superlattices (Donetsky *et al.*, 2010, 2009; Pellegrino and DeWames, 2009) and developing methods for increasing carrier lifetime.

6. CONCLUSIONS AND OUTLOOK

Remarkable progress has been achieved in the antimonide superlattices since the analysis by Smith and Mailhiot (1987) first pointed out their advantages for infrared detection. In the LWIR, type-II InAs/Ga(In)Sb

superlattices have been shown theoretically to have reduced Auger recombination and suppressed band-to-band tunneling. Suppressed tunneling in turn allows for higher doping in the absorber, which has led to reduced diffusion dark current. The versatility of the antimonide material system, with the availability of three different types of band offsets, provides great flexibility in device design. Heterostructure designs that make effective use of unipolar barriers have demonstrated strong reduction of G-R dark current. As a result, the dark current performance of antimonide superlattice-based single element LWIR detectors is now approaching that of the state-of-the-art MCT detector. To date, the antimonide superlattices still have relatively short carrier lifetimes; this issue needs to be resolved before type-II superlattice infrared detectors can achieve their true potential. The antimonide material system has relatively good mechanical robustness when compared with II–VI materials; therefore, FPAs based on type-II superlattices have potential advantages in manufacturability. In the MWIR, production-ready simultaneous dual-band FPA has been fabricated (Rehm *et al.*, 2010; Walther *et al.*, 2007). In the LWIR, large-format FPAs have been demonstrated in research laboratories (Gunapala *et al.*, 2010; Manurkar *et al.*, 2010). Improvements in substrate quality and size and reliable surface leakage current suppression methods, such as those based on robust surface passivation or effective use of unipolar barriers, could lead to high-performance large-format LWIR focal plane arrays.

ACKNOWLEDGMENTS

The authors thank S. Bandara, E. R. Blazejewski, E. S. Daniel, R. E. DeWames. W. R. Frensley, D. R. Rhiger, J. N. Schulman, and D. L. Smith for helpful discussions; S. A. Keo, J. M. Mumolo, B. Yang, J. K. Liu, A. Liao, M. C. Lee, and R. T. Ting for assistance; and M. Tidrow, R. Liang, M. Herman, E. Kolawa, and P. Dimotakis for encouragement and support. A part of the research described in this publication was carried out at the Jet Propulsion Laboratory, California Institute of Technology, under a contract with the National Aeronautics and Space Administration. Government sponsorship acknowledged.

REFERENCES

Abdollahi Pour, S., Nguyen, B.-M., Bogdanov, S., Huang, E. K., and Razeghi, M. (2009). *Appl. Phys. Lett.* **95**, 173505.

Ahrenkiel, R. K., and Lundstrom, M. S. (1993). Minority carriers in III-V Semiconductors: Physics and Applications. in: "Semiconductors and Semimetals." edited by Williardson, R. K., Beer, A. C., Weber, E. R. vol. **39**, Academic Press, San Diego, pp. 40–74.

Aifer, E. H., Jackson, E. M., Boishin, G., Whitman, L. J., Vurgaftman, I., Meyer, J. R., Culbertson, J. C., and Bennett, B. R. (2003). *Appl. Phys. Lett.* **82**(25), 4411–4413.

Aifer, E. H., Maximenko, S. I., Yakes, M. K., Yi, C., Canedy, C. L., Vurgaftman, I., Jackson, E. M., Nolde, J. A., Affouda, C. A., Gonzalez, M., Meyer, J. R., Clark, K. P., and Pinsukanjana, P. R. (2010b). *Proc. SPIE* **7660**, 76601Q.

Aifer, E. H., Tischler, J. G., Warner, J. H., Vurgaftman, I., Bewley, W. W., Meyer, J. R., Kim, J. C., Whitman, L. J., Canedy, C. L., and Jackson, E. M. (2006). *Appl. Phys. Lett.* **89**, 053519.

Aifer, E. H., Tischler, J. G., Warner, J. H., Vurgaftman, I., Kim, J. C., Meyer, J. R., Bennett, B. R., and Whitman, L. J. (2005). *Proc. SPIE* **5732**, 259.

Aifer, E. H., Warner, J. H., Canedy, C. L., Vurgaftman, I., Jackson, E. M., Tischler, J. G., Meyer, J. R., Powell, S. P., Olver, K., Tennant, W. E. (2010a). *J. Electron. Mater.* **39**(7), 1070–1079.

Aifer, E. H., Warner, J. H., Stine, R. R., Vurgaftman, I., Canedy, C. L., Jackson, E. M., Tischler, J. G., Meyer, J. R., Petrovykh, D. Y., and Whitman, L. J. (2007). *Proc. SPIE* **6542**, 654203-1.

Alferov, Zh. I., and Kazarinov, R. F. (1963). Semiconductor Laser with Electric Pumping. Inventor's Certificate No. 181737 (in Russian), Application No. 950 840.

Anderson, R. L. (1962). *Solid State Electron.* **5**(5), 341–344.

Arias, J. M., Pasko, J. G., Zandian, M., Shin, S. H., Williams, G. M., Bubulac, L. O., De Wames, R. E., and Tennant, W. E. (1991). *Appl. Phys. Lett.* **62**(9), 76.

Bennett, B. R. (1998). *Appl. Phys. Lett*. **73**(25), 3736–3738.

Bennett, B. R., Magno, R., Boos, J. B., Kruppa, W., and Ancona, M. G. (2005). *Solid State Electron*. **49**(12), 1875–1895.

Bennett, B. R., Shanabrook, B. V., and Twigg, M. E. (1999). *J. Appl. Phys*. **85**(4), 2157–2161.

Bertru, N., Baranov, A. N., Cuminal, Y., Boisser, G., Alibert, C., and Joullie, A. (1999). *J. Appl. Phys.* **85**, 1989–1991.

Bracker, A. S., Nosho, B. Z., Barvosa-Carter, W., Whitman, L. J., Bennett, B. R., Shanabrook, B. V., and Culbertson, J. C. (2001). Appl. Phys. Lett. **78**(17), 2440–2442.

Brown, E. R., Söderström, J. R., Parker, C. D., Mahoney, L. J., Molvar, K. M., and McGill, T. C. (1991). *Appl. Phys. Lett.* **58**(20), 2291–2293.

Brown, G. J., Szmulowicz, F., Linville, R., Saxler, A., Mahalingham, K., Lin, C.-H., Kuo, C. H., and Hwang, W. Y. (2000). *IEEE Phot. Tech. Lett.* **12**(6), 684–686.

Bürkle, L., and Fuchs, F. (2002). InAs/(GaIn)Sb superlattices: a promising material system for infrared detection. in: "Handbook of Infrared Detection Technologies." edited by Henini, M., Razeghi, M. Elsevier Science, Oxford, pp. 159–189.

Bürkle, L., Fuchs, F., Schmitz, J., and Pletschen, W. (2000). *Appl. Phys. Lett.* **77**, 1659–1661.

Canedy, C. L., Abell, J., Bewley, W. W., Aifer, E. H., Kim, C. S., Nolde, J. A., Kim, M., Tischler, J. G., Lindle, J. R., Jackson, E. M., Vurgaftman, I., and Meyer, J. R. (2010). *J. Vac. Sci. Technol. B: Microelectron. Process. Phenom.* **28**(3), C3G8.

Canedy, C. L., Aifer, E. H., Vurgaftman, I., Tischler, J. G., Meyer, J. R., Warner, J. H., and Jackson, E. M. (2007). *J. Electron. Mater.* **36**(18), 852–856.

Canedy, C. L., Aifer, E. H., Warner, J. H., Vurgaftman, I., Jackson, E. M., Tischler, J. G., Powell, S. P., Olver, K., Meyer, J. R., and Tennant, W. E. (2009). *Infrared Phys. Technol*. **52**(6), 326–334.

Canedy, C. L., Bewley, W. W., Kim, C. S., Kim, M., Vurgaftman, I., and Meyer, J. R. (2003). *J. Appl. Phys.* **94**, 1347–1355.

Carras, M., Reverchon, J. L., Marre, G., Renard, C., Vinter, B., Marcadet, X., and Berger, V. (2005). *Appl. Phys. Lett.* **87**(10), 102103.

Cartoixà, X., Ting, D. Z.-Y., and McGill, T. C. (2003). *Phys. Rev. B: Solid State* **68**(23), 235319.

Chang, Y.-C., and Schulman, J. N. (1985). *Phys. Rev. B: Solid State* **31**(4), 2069–2079.

Chow, D. H., Miles, R. H., Collins, D. A., Schulman, J. N., and McGill, T. C. (1991). *Semicond. Sci. Technol*. **6**, C47–C51.

Ciesla, C. M., Murdin, B. N., Pidgeon, Stradling, C. R., Philips, R. A., M. Livingstone, C. C., Galbraith, I., Jaroszynski , D. A., Langerak, C. J. G. M., Tang P. J. P., and Pullin, M. J., (1996). *J. Appl. Phys*. **80**(5), 2994-2997.

Connelly, B. C., Metcalfe, G. D., Shen, H., and Wraback, M. (2010). *Appl. Phys. Lett.* **97**(25), 251117.

Daniel, E. S., Cartoixà, X., Frensley, W. R., Ting, D. Z.-Y., and McGill, T. C. (2000). *IEEE Trans. Electron Devices* **47**(5), 1052–1060.

Das, S. D., Goh, Y. L., Tan, C. H., David, J. P. R., Rodriguez, J.-B., Plis, E. A., Sharma, Y. D., Kim, H. S., and Krishna, S. (2008). *Proc. SPIE* **7113**, 711301–1.

Davies, J. H. (1998). "The Physics of Low Dimensional Semiconductors: An Introduction." Cambridge University Press, Cambridge, New York, and Melbourne.
Delaunay, P.-Y., Hood, A., Nguyen, B. M., Hoffman, D., Wei, Y., and Razeghi, M. (2007a). *Appl. Phys. Lett.* **91**, 091112.
Delaunay, P.-Y., Nguyen, B. M., Hoffman, D., and Razeghi, M. (2007b). *Proc. SPIE* **6542**, 654204–1.
Delaunay, P.-Y., Nguyen, B. M., Hoffman, D., and Razeghi, M. (2007c). *Appl. Phys. Lett.* **91**, 231106.
Delaunay, P.-Y., Nguyen, B. M., Hoffman, D., and Razeghi, M. (2008). *IEEE J. Quantum Electron.* **44**(5), 462–467.
Delaunay, P.-Y., Nguyen, B. M., Hoffman, D., Huang, E. K., and Razeghi, M. (2009). *IEEE J. Quantum Electron.* **45** (2), 157–162.
Delaunay, P.-Y., and Razeghi, M., (2009). *J. Appl. Phys.* **106**, 063110.
Donetsky, D., Belenky, G., Svensson, S., and Suchalkin, S. (2010). *Appl. Phys. Lett.* **97**(5), 052108.
Donetsky, D., Svensson, S. P., Vorobjev, L. E., and Belenky, G. (2009). *Appl. Phys. Lett.* **95**(21), 212104.
Dragoman, D., and Dragoman, M. (2002). "Optical Characterization of Solids." Springer-Verlag, Berlin, Heidelberg and New York.
Edwall, D. D., DeWames, R. E., McLevige, W. V., Pasko, J. G., and Arias, J. M. (1998). *J. Electron. Mater.* **27**(6), 698.
Esaki, L., and Tsu, R. (1970). *IBM J. Res. Dev*. **14**, 61–65.
Feenstra, R. M., Collins, D. A., Ting, D. Z.-Y., Wang, M. W., and McGill, T. C. (1994a). *Phys. Rev. Lett*. **72**(17), 2749–2752.
Feenstra, R. M., Collins, D. A., Ting, D. Z.-Y., Wang, M. W., and McGill, T. C. (1994b). *J. Vac. Sci. Technol. B: Microelectron. Process. Phenom.* **12**(4), 2592–2597.
Flatte, M. E., and Grein, C. H. (2009). *Proc. SPIE* **7222**, 72220Q.
Frensley, W. R., and Kroemer, H. (1977). *Phys. Rev. B: Solid State* **16**, 2642–2652.
Fuchs, F., Ahlswede, E., Weimar, U., Pletschen, W., and Schmitz, J., Hartung, M., Jager, B., and Szmulowicz, F. (1998b). *Appl. Phys. Letts*. **73**(25), 3760–3762.
Fuchs, F., Bürkle, L., Pletschen, W., Schmitz, J., and Walther, M., (1999). *Proc. SPIE* **3794**, 41–46.
Fuchs, F., Hoffman, D., Gin, A., Hood, A., Wei, Y., and Razeghi, M. (2006). *Phys. Stat. Sol.* (c) **3**, 444–447.
Fuchs, F., Kheng, K., Schwarz, K., and Koidl, P. (1993). *Semicond. Sci. Technol*. **8,** S75–S80.
Fuchs, F., Wagner, J., Schmitz, J., Herres, N., and Koidl, P. (1997b). Growth and Characterization of InAs/AlSb/GaSb Heterostructures. in: "Antimonide-Related Strained-Layer Heterostructures," edited by Manasreh, M. O., Gordon Breach Science Publishers, Amsterdam, pp. 191–232.
Fuchs, F., Weimar, U., Ahlswede, E., Pletschen, W., Schmitz, J., and Walther, M. (1998a). *Proc. SPIE* **3287**, 14–21.
Fuchs, F., Weimer, U., Pletschen, W., Schmitz, J., Ahlswere, E., Walter, M., Wagner, J., and Koidl, P. (1997a). *Appl. Phys. Lett.* **71**(22), 3251–3253.
Gautam, N., Kim, H. S., Kutty, M. N., Plis, E., Dawson, L. R., and Krishna, S. (2010). *Appl. Phys. Lett.* **96**, 231107.
Gendron, L., Carras, M., Huynh, A., Ortiz, V., Koeniguer, C., and Berger, V. (2004). *Appl. Phys. Lett.* **85**, 2824–2826.
Grein, C. H., and Ehrenreich, H. (1997). *J. Appl. Phys*. **82**(12), 6365–6367.
Grein, C. H., Laub, W. H., Harbertb, T. L., and Flatte, M. E. (2002). *Proc. SPIE* **4795**, 39–43.
Grein, C. H., Young, P. M., and Ehrenreich, H. (1992). *Appl. Phys. Lett.* **61**(24), 2905–2907.
Grein, C. H., Young, P. M., Flatte, M. E., and Ehrenreich, H. (1995). *J. Appl. Phys*. **78**(12), 7143–7152.

Gunapala, S. D., Ting, D. Z., Hill, C. J., Nguyen, J., Soibel, A., Rafol, S. B., Keo, S. A., Mumolo, J. M., Lee, M. C., Liu, J. K., Yang, B., and Liao, A., (2010). *Proc. SPIE* **7808**, 780802.
Harrison, W. A. (1977). *J. Vac. Sci. Technol.* **14**, 1016–1021.
Haugan, H. J., Brown, G. J., Pacley, S. D., Grazulis, L., and Fenstermaker, S. T. (2010). *Proc. SPIE* **7808**, 780806–1.
Haugan, H. J., Elhmari, S., Szmulowicz, F., Ullrich, B., Brown, G. J., and Mitchel, W. C. (2008). *Appl. Phys. Lett.* **92,** 071102–1–071102–3.
Haugan, H. J., Szmulowicz, F., Brown, G. J., Ullrich, B., Munshi, S. R., Grazulis, L., Mahalingam, K., and Fenstermaker, S. T. (2006). *Physica E* **32**, 289–292.
Herrera, M., Chi, M., Bonds, M., Browning, N. D., Woolman, J. N., Kvaas, R. E., Harris, S. F., Rhiger, D. R., and Hill, C. J. (2008). *Appl. Phys. Lett.* **93**, 093106.
Herres, N., Fuchs, F., Schmitz, J., Pavlov, K. M., Wagner, J., Ralston, J. D., and Koidl, P. (1996). *Phys. Rev. B*. **53**(23), 15688–15705.
Hill, C. J., Soibel, A., Keo, S. A., Mumolo, J. M., Ting, D. Z., and Gunapala, S. D. (2009b). *Proc. SPIE*, **7298**, 729804–1.
Hill, C. J., Soibel, A., Ting, D. Z.-Y., Keo, S. A., Mumolo, J. M., Nguyen, J., Lee, M., and Gunapala, S. D. (2009a). *Electron. Lett.* **45**(21), 1089–1090.
Hitchcock, C. W., Gutmann, R. J., Borrego, J. M., Bhat, I. B., and Charache, G. W. (1999). *IEEE Trans. Electron Devices* **46**(10), 2154–2161.
Hoffman, D., Gin, A., Wei, Y., Hood, A., Fuchs, F., and Razeghi, M. (2005). *IEEE J. Quantum Electron.* **41**, 1474–1479.
Hoffman, D., Hood, A., Michel, E., Fuchs, F., and Razeghi, M. (2006). *IEEE J. Quantum Electron.* **42**, 126–130.
Hoffman, D., Nguyen, B.-M., Delaunay, P.-Y., Hood, A., and Razeghi, M. (2007). *Appl. Phys. Lett.* **91**, 143507.
Hoffman, D., Nguyen, B.-M., Huang, E. K., Delaunay, P.-Y., Razeghi, M., Tidrow, M. Z., and Pellegrino, J. (2008). *Appl. Phys. Lett.* **93**, 031107.
Höglund, L., Soibel, A., Hill, C. J., Ting, D. Z., Khoshaklagh, A., Liao, A., Keo, S., Lee, M. C., Nguyen, J., Mumolo, J. M., Gunapala, S. D. (2010). *Proc. of SPIE* **7780**, 77800D.
Hood, A., Delaunay, P.-Y., Hoffman, D., Nguyen, B.-M., Wei, Y., and Razeghi, M. (2007). *Appl. Phys. Lett.* **90**, 233513.
Hood, A. D., Evans, A. J., Ikhlassi, A., Lee, D. L., and Tennant, W. E. (2010a). *J. Electron. Mater.* **39**(7), 1001–1006.
Hood, A., Evans, A. J., Ikhlassi, A., Sullivan, G., Piquette, E., Lee, D. L., Tennant, W. E., Vurgaftman, I., Canedy, C. L., Jackson, E. M., Nolde, J. A., Yi, C., and Aifer, E. H. (2010b). *Proc. SPIE* **7660**, 76601M-1.
Hood, A., Razeghi, M., Aifer, E. H., and Brown, G. J. (2005b). *Appl. Phys. Lett.* **87**, 151113.
Hood, A., Wei, Y., Gin, A., Razeghi, M., Tidrow, M. Z., and Nathan, V. (2005a). *Proc. SPIE* **5732**, 316.
Huang, E. K., Hoffman, D., Nguyen, B.-M., Delaunay, P.-Y., and Razeghi, M. (2009). *Appl. Phys. Lett.* **94**, 053506.
Johnson, J. L., Samoska, L. A., Gossard, A. C., Merz, J. L., Jack, M. D., Chapman, G. R., Baumgratz, B. A., Kosai, K., and Johnson, S. M. (1996). *J. Appl. Phys.* **80**(2), 1116–1127.
Kane, E. O. (1957). *J. Phys. Chem. Solids* **1**, 249–261.
Kaspi, R., Moeller, C., Ongstad, A., Tilton, M. L., Gianardi, D., Dente, G., and Gopaladasu, P. (2000). *Appl. Phys. Lett.* **76**, 409–411.
Khoshakhlagh, A., Plis, E., Myers, S., Sharma, Y. D., Dawson, L. R., and Krishna, S. (2009). *J. Cryst. Growth* **311**, 1901–1904.
Khoshakhlagh, A., Rodriguez, J. B., Plis, E., Bishop, G. D., Sharma, Y. D., Kim, H. S., Dawson, L. R., and Krishna, S. (2007). *Appl. Phys. Lett.* **91**, 263504.
Kim, H. S., Plis, E., Myers, S., Khoshakhlagh, A., Gautam, N., Kutty, M. N., Sharma, Y. D., Dawson, L. R., and Krishna, S. (2009). *Proc. SPIE* **7467**, 74670U–1.

Kim, H. S., Plis, E., Rodriguez, J. B., Bishop, G. D., Sharma, Y. D., Dawson, L. R., Krishna, S., Bundas, J., Cook, R., Burrows, D., Dennis, R., Patnaude, K., Reisinger, A., and Sundaram, M. (2008). *Appl. Phys. Lett.* **92**(18), 183502.

Kim, J. C., Tischler, J. G., Canedy, C. L., Aifer, E. H., Vurgaftman, I., Vurgaftman, I., Meyer, J. R., and Whitman, L. J. (2007). *J. Cryst. Growth* **303**(2), 515–519.

Kinch, M. A. (2000). *J. Electron. Mater.* **29,** 809–817.

Kinch, M. A. (2007). "Fundamentals of Infrared Detector Materials." SPIE Press, Bellingham.

Kinch, M. A., Aqariden, F., Chandra, D., Liao, P.-K., Schaake, H. F., and Shih, H. D. (2005). *J. Electron. Mater.* **34**(6), 880.

Klin, O., Grossman, S., Snapi, N., Brumer, M., Lukomsky, I., Yassen, M., Yofis, B., Glozman, A., Zemel, A., Fishman, T., Berkowitz, E., Magen, O., Oiknine-Schlesinger, J., Shtrichman, I., Weiss, E., and Klipstein, P. C. (2009). *Proc. SPIE* **7298**, 7298–0G.

Klipstein, P. C. (2005). Depletion-less photodiode with suppressed dark current and method for producing the same. Int. Patent Publication no: WO 2005/004243 A1 (13 January 2005, priority date: 2 July 2003).

Klipstein, P. C. (2008). *Proc. SPIE* **6940**, 69402U.

Klipstein, P. C., Klin, O., Grossman, S., Snapi, N., Yaakobovitz, B., Brumer, M., Lukomsky, I., Aranov, D., Yassen, M., Yofis, B., Glozman, A., Fishman, T., Berkowicz, E., Magen, O., Shtrichman, I., and Weiss, E. (2010). *Proc. SPIE* **7608**, 76081V.

Kroemer, H. (1963). *Proc. IEEE* **52**(12), 1782.

Kroemer, H. (2004). *Physica E* **20**, 196.

Kutty, M. N., Plis, E., Khoshakhlagh, A., Myers, S., Gautam, N., Smoley, S., Sharma, Y. D., Dawson, R., Krishna, S., Lee, S. J., and Noh, S. K. (2010). *J. Electron. Mater.* **39**, 10, 2203–2209.

Lacroix, Y., Tran, C. A., Watkins, S. P., Thewalt, M. L. W. (1996). *J. Appl. Phys.* **80**, 6416–6424.

Lew, A. Y., Zuo, S. L., Yu, E. T., and Miles, R. H. (1998). *Phys. Rev. B* **57**(11), 6534–6539.

Li, J. V., Chuang, S. L., Jackson, E. M., and Aifer, M. (2004). *Appl. Phys. Lett.* **85**(11), 1984–1986.

Li, J. V., Yang, R. Q., Hill, C. J., and Chuang, S. L. (2005). *Appl. Phys. Lett.* **86**, 101102.

Liu, C., Hughes, T. L., Qi, X.-L., Wang, K., and Zhang, S.-C. (2008). *Phys. Rev. Lett.* **100**(23), 236601.

Maimon, S. (2010). Reduced dark current photodetector. U.S. Patent No. 7,687,871 B2.

Maimon, S., and Wicks, G. W. (2003). InAsSb/GaAlSb/InAsSb nBn IR detector for the 3–5 μm. in: Abstract Book of the 11th International Conference on Narrow Gap Semiconductors, Buffalo, New York, pp. 70.

Maimon, S., and Wicks, G. W. (2006). *Appl. Phys. Lett.* **89**(15), 151109.

Manurkar, P., Ramezani-Darvish, S., Nguyen, B. M., Razeghi, M., and Hubbs, J. (2010). *Appl. Phys. Lett.* **97**, 193505.

Miles, R. H., Chow, D. H., Schulman, J. N., and McGill, T. C. (1990). *Appl. Phys. Lett.* **57**(8), 801–803.

Miles, R. H., Schulman, J. N., Chow, D. H., and McGill, T. C. (1993). *Semicond. Sci. Technol.* **8**, S102–S105.

Mohseni, H., Litvinov, V. I., and Razeghi, M. (1998b). *Phys. Rev. B.*, **58**(23) 15378–15380.

Mohseni, H., Michel, E., Razeghi, M., Mitchel, W., and Brown, G. (1998a). *Proc. SPIE* **3287**, 30–37.

Mohseni, H., and Razeghi, M. (2001). *IEEE Photonics Technol. Lett.* **13**, 517–519.

Mohseni, H., Razeghi, M., Brown, G., and Park, Y. S. (2001), *Appl. Phys. Lett.* **78**(15), 2107–2109.

Mohseni, H., Wojkowski, J., Razeghi, M., Brown, G., and Mitchel, W. (1999). *IEEE J. Quantum Electron.* **35**(7), 1041–1044.

Mohseni, H., Wojkowski, J. S., Tahraoui, A., Razeghi, M., Brown, G., and Mitchel, W. (2000). *Proc. SPIE* **3948**, 153–160.

Moyer, H. P., Schulman, J. N., Lynch, J. J., Schaffner, J. H., Sokolich, M., Royter, Y., Bowen, R. L., McGuire, C. F., Hu, M., Schmitz, A. (2008). *IEEE Microwave Wireless Compon. Lett.* **18**(10) 686–688.

Nguyen, B.-M., Bogdanov, S., Abdollahi Pour, S., and Razeghi, M. (2009a). *Appl. Phys. Lett.* **95**(18), 183502.

Nguyen, B.-M., Hoffman, D., Delaunay, P.-Y., Huang, E. K.-W., Razeghi, M., and Pellegrino, J. (2008b). *Appl. Phys. Lett.* **93**(16), 163502.

Nguyen, B.-M., Hoffman, D., Delaunay, P.-Y., and Razeghi, M. (2007b). *Appl. Phys. Lett.* **91**(16), 163511.

Nguyen, B. M., Hoffman, D., Huang, E. K., Bogdanov, S., Delaunay, P.-Y., Razeghi, M., and Tidrow, M. Z. (2009b). *Appl. Phys. Lett.* **94**, 223506.

Nguyen, B.-M., Hoffman, D., Huang, E. K.-W., Delaunay, P.-Y., and Razeghi, M. (2008a). *Appl. Phys. Lett.* **93**(12), 123502.

Nguyen, J., Hill, C. J., Rafol, D., Keo, S. A., Soibel, A., Ting, D. Z.-Y., Mumolo, J. M., Liu, J. K., and Gunapala, S. D. (2010a). *Proc. SPIE* **7945**, 7945–67.

Nguyen, B.-M., and Razeghi, M. (2007a). *Proc. SPIE* **6479**, 64790S–1.

Nguyen, J., Soibel, A., Ting, D. Z.-Y., Hill, C. J., Lee, M. C., and Gunapala, S. D. (2010b). *Appl. Phys. Lett.* **97**, 051108.

Nguyen, J., Ting, D. Z.-Y., Hill, C. J., Soibel, A., and Gunapala, S. D. (2009c). *Infrared Phys. Technol.* **52**(6), 317–321.

Niles, D. W., and Margaritondo, G. (1986). *Phys. Rev. B* **34**, 2923–2925.

Ongstad, A. P., Dente, G. C., Tilton, M. L., Gianardi, D., and Turner, G. (2000). *J. Appl. Phys.* **87**, 7896–7902.

Pavesi, L., and Guzzi, M. (1994). *J. Appl. Phys.* **75,** 4779–4842.

Pedrazzani, J. R., Maimon, S., and Wicks, G. W. (2008). *Electron. Lett.* **44**(25), 1487–1488.

Pellegrino, J., DeWames, R. (2009). *Proc. SPIE* **7298**, 72981U-4.

Plis, E., Annamalai, S., Posani, K. T., Krishna, S., Rupani, R. A., and Ghosh, S. (2006). *J. Appl. Phys.* **100**, 014510–1–014510–4.

Plis, E., Kim, H. S., Bishop, G., Krishna, S., Banerjee, K., Ghosh, S. (2008). *Appl. Phys. Lett.* **93**(12), 123507.

Plis, E., Rotella, P., Raghavan, S., Dawson, L. R., Krishna, S., Le, D., and Morath, C. P. (2003). *Appl. Phys. Lett* **82**(11), 1658–1660.

Pultz, G. N., Norton, P. W., Kruger, E. E., and Reine, M. B. (1991). *J. Vac. Sci. Technol. B: Microelectron. Process. Phenom.* **9**(3), 1724–1730.

Razeghi, M., Huang, E. K., Nguyen, B.-M., Pour, S. A., and Delaunay, P.-Y. (2010). *Proc. SPIE* **7660**, 76601F-1.

Razeghi, M., and Mohseni, F. (2002). GaSb/InAs superlattices for infrared FPAs. in: "Handbook of Infrared Detection Technologies" edited by Henini, M., and Razeghi, M., Elsevier Science, Oxford, pp. 191–232.

Rehm, R., Walther, M., Fuchs, F., Schmitz, J., and Fleissner, J. (2005). *Appl. Phys. Lett.* **86**, 173501.

Rehm, R., Walther, M., Schmitz, J., FleiBner, J., Fuchs, F., Ziegler, J., and Cabanski, W. (2006). *Opto-Electronics Rev.* **14**, 19.

Rehm, R., Walther, M., Schmitz, J., Rutz, F., and Wörl, A. (2010). *Proc. SPIE* **7660**, 76601G.

Reverchon, J. L.,Carras, M., Marre, G., Renard, C., Berger, V., Vinter, B., and Marcadet, X. (2004). *Physica E* **20**(3–4), 519–522.

Rhiger, D. R., Kvaas, R. E., Harris, S. F., and Hill, C. J. (2009). *Infrared Phys. Technol.* **52**(6), 304–309.

Rhiger, D. R., Kvaas, R. E., Harris, S., Bornfreund, R. E., Thai, Y. N., Hill, C. J., Li, J. V., Gunapala, S. D., and Mumolo, J. M., (2007). *Proc/ SPIE* **6542**, 654202–1.

Rhiger, D. R., Kvaas, R. E., Harris, S. F., Kolasa, B. P., Hill, C. J., and Ting, D. Z. (2010). *Proc. SPIE* **7660**, 76601N.

Rodriguez, J. B., Christol, P., Chevrier, F., and Joullie, A. (2005). *Physica E* **28**, 128–133.

Rodriguez, J. B., Plis, E., Bishop, G., Sharma, Y. D., Kim, H., Dawson, L. R., and Krishna, S. (2007). *Appl. Phys. Lett.* **91**(4), 043514.

Rogalski, A. (2011). "Infrared Detectors." CRC Press, Boca Raton.

Sai-Halasz, G. A., Chang, L. L., Welter, J.-M., Chang, C. A., and Esaki, L., (1978b). *Solid State Commun.* **27**(10), 935–937.

Sai-Halasz, G. A., Esaki, L., and Harrison, W. A. (1978a). *Phys. Rev. B* **18**(6), 2812–2818.

Sai-Halasz, G. A., Tsu, R., and Esaki, L. (1977). *Appl. Phys. Lett.* **30**(12), 651–653.

Sakaki, H., Chang, L. L., Ludeke, R., Chang, C. A., Sai-Halasz, G. A., and Esaki, L. (1977). *Appl. Phys. Lett.* **31**(3), 211–213.

Savich, G. R., Pedrazzani, J. R., Maimon, S., Wicks, G. W. (2010). *J. Vac. Sci. Technol. B: Microelectron. Process. Phenom.* **28**(3), C3H18–C3H21.

Schmitz, J., Wagner, J., Fuchs, F., Herres, N., Koidl, P., and Ralston, J. D. (1995). *J. Cryst. Growth* **150**, 858–862.

Schulman, J. N., and Chang, Y.-C. (1985). *Phys. Rev. B* **31**(4), 2056–2068.

Schulman, J. N., and McGill, T. C. (1979a). *Appl. Phys. Lett.* **34**(10), 663–665.

Schulman, J. N., and McGill, T. C. (1979b). *J. Vac. Sci. Technol. B: Microelectron. Process. Phenom.* **16**, 1513–1516.

Schulman, J. N., Holabird, K. S., Chow, D. H., Dunlap, H. L., Thomas, S., and Croke, E. T. (2002). *Electron. Lett.* **38**(2), 94–95.

Shterengas, S. L., Belenky, G., Kisin, M. V., and Donetsky, D. (2007). *Appl. Phys. Lett.* **90**(1), 011119, and references therein.

Smith, D. L., Mailhiot, C. (1987). *Appl. Phys. Lett.* **34**(10), 663–665.

Smith, D. L., McGill, T. C., and Schulman, J. N. (1983). *Appl. Phys. Lett.* **43**(2), 180–182.

Söderström, J. R., Chow, D. H., and McGill, T. C. (1989). *Appl. Phys. Lett.* **55**(11), 1094–1096.

Soibel, A., Ting, D. Z.-Y., Hill, C. J., Lee, M., Nguyen, J., Keo, S. A., Mumolo, J. M., and Gunapala, S. D. (2010). *Appl. Phy. Lett.* **96**(11), 111102.

Steinshnider, J., Harper, J., Weimer, M., Lin, C.-H., Pei, S.-S., and Chow, D. H. (2000b). *Phys. Rev. Lett.* **85**(21), 4562–4565.

Steinshnider, W. M., Kaspi, R., and Turner, G. W. (2000a). *Phys. Rev. Lett.* **85**(14), 2953–2956.

Sze, S. M., and Ng, K. K. (2007). "Physics of Semiconductor Devices, 3rd edition." Wiley, New Jersey.

Tan, S. L., Goh, Y. L., Das, S. D., Zhang, S., Tan, C. H., David, J. P. R., Gautam, N., Kim, H., Plis, E., and Krishna, S. (2010). *Proc. SPIE* **7838**, 783814–1.

Tennant, W. E. (2010). *J. Electron. Mater.* **39**(7), 1030.

Tennant, W. E., Lee, D., Zandian, M., Piquette, E., and Carmody, M. (2008). *J. Electron. Mater.* **37**(9), 1406.

Terterian, S., Nosho, B., Sharifi, H., Patterson, P., and Rajavel, R. (2010). *Proc. SPIE* **7660**, 76601O-1.

Ting, D. Z., Bandara, S. V., Hill, C. J., and Gunapala, S. D. (2009c). *NASA Tech. Briefs* **33**(6), 57–58.

Ting, D. Z.-Y., Bandara, S. V., Mumolo, J., Keo, S. A., Nguyen, J., Liu, H. C., Song, C. Y., Chang, Y.-C., Rafol, S. B., Hill, C. J., Gunapala, S. D., Soibel, A., Liu, J. K., and Blazejewski, E. (2009b). *Infrared Phys. Technol.* **52**(6), 294–298.

Ting, D. Z.-Y., and Cartoixà, X. (2002). *Appl. Phys. Lett.* **81**(22), 4198–4200.

Ting, D. Z.-Y., and Cartoixà, X. (2003). *Appl. Phys. Lett.* **83**(7), 1391–1393.

Ting, D. Z.-Y., Collins, D. A., Yu, E. T., Chow, D. H., and McGill, T. C. (1990). *Appl. Phys. Lett.* **57**(12), 1257–1259.

Ting, D. Z.-Y., Hill, C. J., Soibel, A., Keo, A., Mumolo, J. M., Nguyen, J., and Gunapala, S. D. (2009a). *Appl. Phys. Lett.* **95**(2), 023508.

Ting, D. Z.-Y., Hill, C. J., Soibel, A., Nguyen, J., Keo, S. A., Mumolo, J. M., Lee, M. C., Yang, B., and Gunapala, S. D. (2010). *Proc. SPIE* **7419**, 74190B.

Tung, T., DeArmond, L. V., Herald, R. F., Herning, P. E., Kalisher, M. H., Olson, D. A., Risser, R. F., Stevens, A. P., and Tighe, S. J. (1992). *Proc. SPIE* **1735**, 109.
van der Ziel, A. (1970). *Proc. IEEE* **58**, 1178–1206.
Vurgaftman, I., Aifer, E. H., Canedy, C. L., Tischler, J. G., Meyer, J. R., Warner, J. H., Jackson, E. M., Hildebrandt, G., Sullivan, G. J. (2006). *Appl. Phys. Lett.* **89**(12), 121114.
Vurgaftman, I., Meyer, J. R., Ram-Mohan, L. R. (2001). *J. Appl. Phys.* **89**(11), 5815–5875.
Wagner, J., Schmitz, J., Herres, N., Fuchs, F., and Walther, M. (1998). *J. Appl. Phys*. **83**(10), 5452–5457.
Walther, M., Rehm, R., FleiBner, J., Schmitz, J., Ziegler, J., Cabanski, W., and Breiter, R. (2007). *Proc. SPIE* **6542**, 654206–1.
Walther, M., Rehm, R., Fuchs, F., Schmitz, J., Fleißner, J., Cabanski, W., Eich, D., Finck, M., Rode, W., Wendler, J., Wollrab, R., Ziegler, J. (2005b). *J. Electron. Mater.* **34**(6), 722–725.
Walther, M., Schmitza, J., Rehma, R., Koptaa, S., Fuchs, F., Fleibnera, J., Cabanskib, W., and Ziegler, J. (2005a). *J. Cryst. Growth* **278**(156–161).
Wang, C. A., Choi, H. K., Ransom, S. L., Charache, G. W., Danielson, L. R., and DePoy, D. M. (1999). *Appl. Phys. Lett.* **75**(9), 1305–1307.
Wei, Y., Gin, A., Razeghi, M., and Brown, G. J. (2002a). *Appl. Phys. Lett*. **80**(18), 3262–3264.
Wei, Y., Gin, A., Razeghi, M., and Brown, G. J. (2002b). *Appl. Phys. Lett*. **81**(19), 3675–3677.
Wei, Y., Hood, A., Yau, H., Yazdanpanah, V., Razeghi, M., Tidrow, M. Z., and Nathan, V. (2005). *Appl. Phys. Lett.* **86**, 091109.
White, A. M. (1987). Infra red detectors. U. S. Patent No. 4,679,063.
Wicks, G. W., Savich, G. R., Pedrazzani, J. R., Maimon, S. (2010). *Proc. SPIE* **7608**, 760822.
Xie, Q., Nostrand, J. E. V., Brown, J. L., and Stutz, C. E. (1999). *Phys. Rev. B*. **86**(1), 329–337.
Yang, R. Q. (1995). *Superlattices Microstruct.* **17**(1), 77–83.
Yang, Q. K., Fuchs, F. Schmitz, J., and Pletschen, W. (2002). *Appl. Phys. Lett.* **81**, 4757–4759.
Yang, R. Q., Hill, C. J., Mansour, K., Qiu, Y., Soibel, A., Muller, R. E., and Echternach, P. M. (2007). *IEEE J. Sel. Top. Quantum Electron.* **13**(5) 1074–1078.
Yang, Q. K., Pfahler, C., Schmitz, J., Pletschen, W., and Fuchs, F. (2003). *Proc. SPIE* (4999) 448–456.
Yang, R. Q., Tian, Z., Cai, Z., Klem, J. F., Johnson, M. B., and Liu, H. C. (2010b). *J. Appl. Phys.* **107**, 054514.
Yang, R. Q., Tian, Z., Klem, J. F., Mishima, T. D., Santos, M. B., and Johnson, M. B. (2010a). *Appl. Phys. Lett.* **96**, 063504.
Youngsdale, E. R., Meyer, J. R., Hoffman, C. A., Bartoli, F. J., Grein, C. H., Young, P. M., Ehrenreich, H., Miles, R. H., and Chow, D. H. (1994). *Appl. Phys. Lett.* **64**(23), 3160–3162.